Actomyosin-mediated apical constriction promotes physiological germ cell death in *C. elegans*

Tea Kohlbrenner[1,2], Simon Berger[1,3], Tinri Aegerter-Wilmsen[1], Ana Cristina Laranjeira[1,2], Andrew deMello[3], Alex Hajnal[1,*]

[1]Institute of Molecular Life Sciences, University of Zürich, Winterthurerstrasse 190, CH-8057 Zürich, Switzerland

[2]Molecular Life Science PhD Program, University and ETH Zürich, CH-8057 Zürich, Switzerland

[3]Institute for Chemical and Bioengineering, ETH Zürich, Vladimir-Prelog-Weg 1-5/10 8093 Zürich, Switzerland

*Corresponding author: alex.hajnal@mls.uzh.ch

Keywords: *C. elegans*, apoptosis, germ cells, MAP kinase, apical constriction, actomyosin network

Abstract

Germ cell apoptosis in *C. elegans* hermaphrodites is a physiological process eliminating around 60% of all cells in meiotic prophase to maintain tissue homeostasis. In contrast to programmed cell death in the *C. elegans* soma, the selection of germ cells undergoing apoptosis is stochastic.

By live-tracking individual germ cells at the pachytene stage, we found that germ cells smaller than their neighbors are selectively eliminated through apoptosis before differentiating into oocytes. Thus, cell size is a strong predictor of physiological germ cell death. The RAS/MAPK and ECT/RHO/ROCK pathways together regulate germ cell size by controlling actomyosin constriction at the apical rachis bridges, which are cellular openings connecting the syncytial germ cells to a shared cytoplasmic core. Enhancing apical constriction reduces germ cell size and increases the rate of cell death while inhibiting the actomyosin network in the germ cells prevents their death. We propose that actomyosin contractility at the rachis bridges of the syncytial germ cells amplifies intrinsic disparities in cell size. Through this mechanism, animals can adapt the rate of germ cell death and differentiation to changing environmental conditions.

Introduction

Programmed cell death, commonly called apoptosis, is an evolutionary conserved process that is essential for the development, morphogenesis and survival of most multicellular organisms [1–4]. During *C. elegans* embryonic and larval development, an invariant set of 131 somatic cells is eliminated through programmed cell death as part of normal development [5–10]. In addition, in adults grown under standard conditions, around 60% of the germ cells at the pachytene stage of meiotic prophase I are eliminated by apoptosis before they can enter oogenesis [11–13]. Germ cell corpses are rapidly engulfed and digested by the somatic sheath cells that form the walls of the tubular gonad arms [11,14,13]. Unlike the programmed death of somatic cells, the death of meiotic germ cells in adult hermaphrodites occurs randomly. The elimination of healthy germ cells by apoptosis is a physiological process that is thought to remove excess cells to maintain tissue homeostasis and redistribute resources among the surviving germ cells [11,15]. While programmed, somatic and physiological germ cell death utilize the same core cell death (CED) machinery to execute apoptosis via CED-3 Caspase activation [5], the signals by which individual germ cells are selected to die have so far remained unknown.

The gonads of *C. elegans* hermaphrodites are formed by two U-shaped tubes each connected to a common uterus [16]. One gonad arm in adult animals contains around 1’000 germ cells arranged in a distal to proximal polarity (**Fig. 1A**) [17]. Germ cells in the distal gonad and the loop region form a large syncytium, in which the germ cell nuclei are only partially enclosed by plasma membranes. Each syncytial germ cell is connected on its apical side through an opening, called rachis bridge, to a common cytoplasmic core, the rachis (**Fig. 1A’ & A’’**) [16]. The rachis bridges are lined with contractile actomyosin rings, which can constrict to close the openings to the rachis, thereby regulating the exchange of cytoplasm between germ cells and rachis [18,19]. The size of the rachis bridges is dynamically regulated according to the meiotic stage of the cells. The rachis bridges first constrict as cells pass through the mid to late pachytene region, after which they enlarge in cells that exit pachytene and enter diakinesis/diplotene in the loop region until they are fully constricted to cellularize the maturing oocytes [19].

Signals transduced by the RHO family of small GTPases regulate cell shape in a variety of processes, including gastrulation, cytokinesis, cell migration and epithelial morphogenesis. In most of these processes, the activation of RHO signaling by extracellular or cell-intrinsic signals induces the constriction of the cortical actomyosin network to generate intracellular

forces, which alter cell shape [20–22]. One of the central downstream effectors is the RHO-dependent kinase ROCK, which induces actomyosin constriction by phosphorylating the regulatory myosin light chain (MLC) subunit. In the *C. elegans* germline, actomyosin contractility is regulated by the RHO Guanine Exchange Factor (GEF) ECT-2 and the RHO-1 small GTPase that activates the ROCK homolog LET-502, which phosphorylates the myosin regulatory light chain MLC-4 [23–25]. Phosphorylated, activated MLC-4 in a complex with the essential light chain MLC-5 and the myosin heavy chain NMY-2 induces constriction of the F-actin cytoskeleton [26]. MLC-4 can also be activated through a RHO/ROCK-independent pathway composed of the p21-activated kinase PAK-1 and its activator PIX-1 [26–28].

Germline stem cells in the distal-most mitotic zone are induced by a DELTA/NOTCH signal from the distal tip cell (DTC) to proliferate (**Fig. 1A**) [17]. As the germ cells migrate proximally, they enter the pachytene stage of meiotic prophase I. While progressing through the pachytene region, germ cells receive external signals via the DAF-2 insulin receptor (InsR), which activates the RAS/MAPK pathway [29]. RAS/MAPK signaling is not only necessary for the surviving germ cells to exit pachytene and differentiate into mature oocytes but also for germ cell death, which occurs almost exclusively in the mid to late pachytene region (**Fig. 1A**) [11,13,30]. The mechanisms, by which MAPK activation triggers the apoptosis of individual germ cells, remain unknown.

Here, we show that RAS/MAPK signaling is necessary for NMY-2 myosin enrichment at the rachis bridges to promote apical germ cell constriction and reduce germ cell size. Smaller germ cells are then selectively eliminated by apoptosis and donate their cytoplasm to surviving germ cells, which grow in size [31,32]. Based on these findings, we propose that global actomyosin contractility in the syncytial germline, determined by the joint activities of the RAS/MAPK and ECT/RHO/ROCK signaling pathways, determines the rate of physiological germ cell death.

Results

Germ cell size decreases before corpse formation

To observe germ cells undergoing apoptosis, we used a custom-made microfluidic device, which allowed us to perform long-term imaging and follow the fates of individual germ cells under physiological conditions [12]. Germ cells in the pachytene stage of meiotic prophase I were tracked over 7 hours in young adult wild-type animals starting 72 hours after the L1 stage, using the *syn-4>syn-4::gfp* membrane marker (*xnIs87*) to outline the cell borders and DIC

optics to visualize apoptotic corpses. Image stacks were acquired every 7.5 minutes, and 2.5D projections of the basal germ cell surfaces were created using MorphographX software [33] (**suppl. Fig. S1C** and the **Extended Methods** section). The basal projections of the consecutive time points were manually aligned, such that individual germ cells could be color-coded and tracked over time (**Fig. 1B-E** and **suppl. Movie S1**).

Analysis of a total of 155 germ cells tracked in three animals revealed that the basal surface area of germ cells undergoing apoptosis decreased prior to the appearance of a cell corpse in the DIC image (time-point 0' in **Fig. 1D**), whereas the surviving neighboring cells increased in size as they moved proximally (**Fig. 1F** and **suppl. Fig. S1A, B**). Relative to their surviving neighbors, cells fated to die started to shrink 1 to 2 hours before apoptotic corpses became visible (**Fig. 1G)**. The average basal area of the 16 apoptotic germ cells that could be tracked until corpse formation was 21±6 μm^2 at the last time frame before they were eliminated. When the basal area dropped below 20 μm^2, cells formed a corpse within an hour with a probability of 58%, compared to a probability of 1% for cells with a basal area greater than 20 μm^2. Therefore, a basal area below 20 μm^2 may serve as a predictor for imminent apoptosis. By creating projections of increasing depths, we found that the basal and apical membrane domains of pre-apoptotic cells decreased simultaneously, while their height did not increase, indicating a reduction in the total volume of pre-apoptotic germ cells (**suppl. Fig. S1D, E**).

Next, we used an endogenous reporter for the non-muscle myosin *nmy-2* (*nmy-2::gfp(cp13)*) [34] to visualize the rachis bridges on the apical side of the syncytial germ cells together with a *pie-1>mCherry::PLCΔ^{PH}* membrane reporter (*itIs37*) to label the plasma membranes. The apical actomyosin rings were fully constricted 30 to 45 minutes before corpse formation, leading to the full cellularization of apoptotic cells before corpse formation (**Fig. 1H-K**). Cellularized germ cells were characterized by a round rather than a honeycomb shape on their basal surface (see the -45' time-point in **Fig. 1C**).

Taken together, our long-term tracking experiments indicated that germ cells fated to die undergo apical constriction and reduce their size 1 to 2 hours before forming apoptotic corpses, which are engulfed by the somatic sheath cells. However, these observations could not distinguish if the reduction in germ cell size is merely a consequence or also a cause of the apoptotic fate.

Figure 1

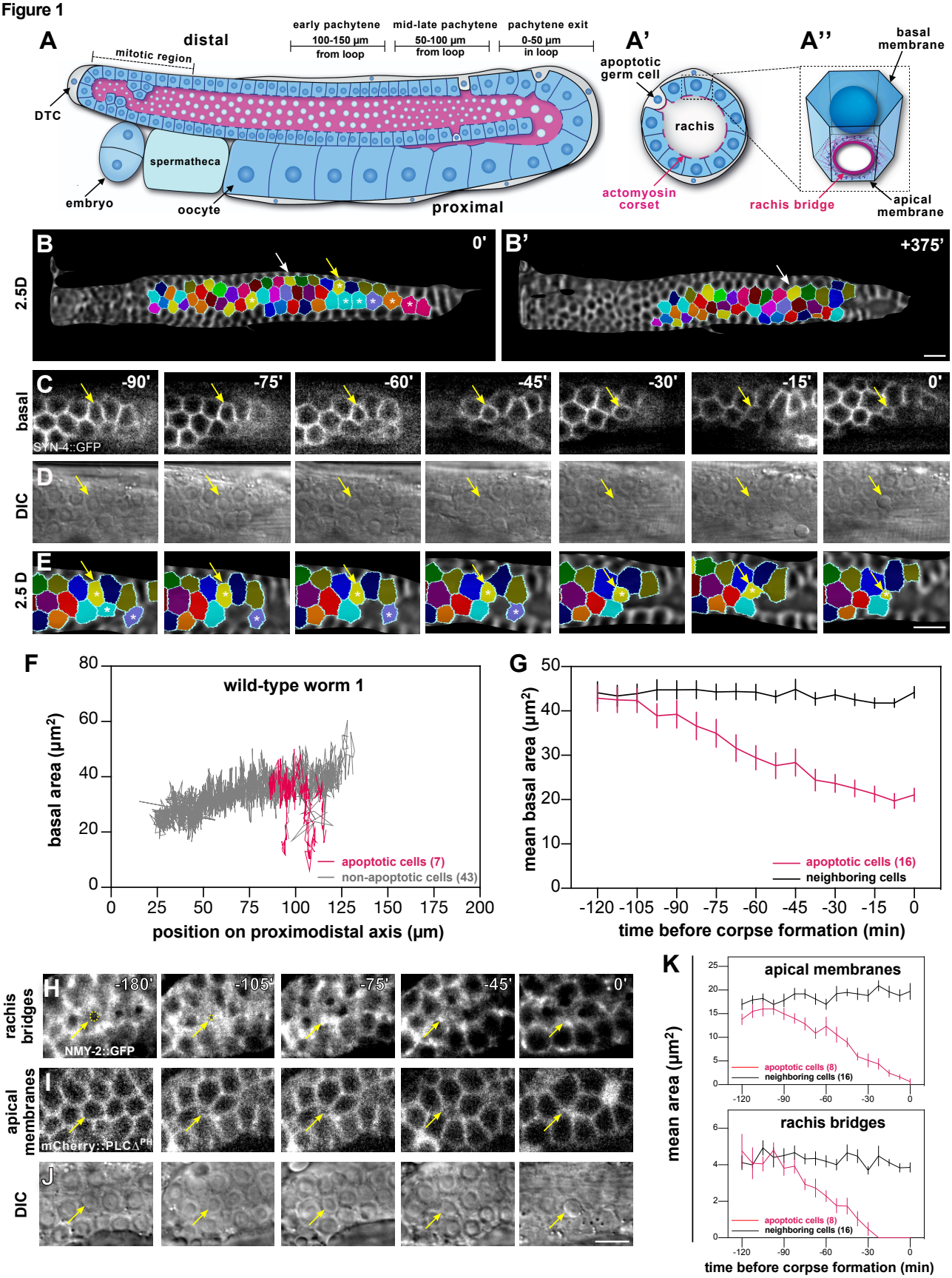

130

Figure 1. Germ cell size decreases before corpse formation.
(**A**) Schematic drawing of a single gonad arm, oriented with its distal end on the top left and the proximal end on the bottom left side, with (**A'**) showing a cross-section through the pachytene region and (**A''**) a single germ cell with its rachis bridge. Live germ cells are indicated with a blue cytoplasm, while the cytoplasm of apoptotic germ cells and the somatic sheath cells are colored gray. The actomyosin corset lining the apical germ cell membranes and the rachis bridges is shown in magenta. The three zones used for measurements in the following figures are indicated as "0-50 µm in the loop" (pachytene exit of survivors), "50-100 µm from the loop" (mid to late pachytene), and "100-150 µm from the loop" (early pachytene). (**B**) Start (0 minutes) and (**B'**) endpoint (+375 minutes) of a germ cell tracking experiment in the wild-type showing the color-coded germ cells in 2.5D projections of the basal membrane surface. See **suppl. Movie S1** for all time frames. The yellow arrow in (**B**) points to a pre-apoptotic germ cell that was tracked as shown in the magnified images in (**C-E**), while the white arrows in (**B**) and (**B'**) point to a surviving germ cell. The white asterisks highlight other cells that underwent apoptosis during the recording. (**C**) shows single z-sections, (**D**) the corresponding DIC images, and (**E**) the segmented cells on the 2.5D projections. (**F**) Basal areas of cells were tracked in a single wild-type animal and plotted against their relative positions along the distal to proximal axis. The traces of apoptotic cells are shown in magenta and those of surviving cells or of cells that did not die during the recording are shown in gray. Therefore, small germ cells in **Fig. 1F** and **suppl. Fig. S1A, B** that could not be tracked until corpse formation are also labeled in black. See **suppl. Fig. S1A, B** for traces of two additional animals. (**G**) Mean basal cell area ±SEM of apoptotic germ cells tracked in three wild-type animals (magenta line) and their neighboring cells (black line) plotted against the relative time before an apoptotic cell corpse was first detected in the DIC channel. Neighboring cells were defined as cells within 16 µm (corresponding to approximately two cell diameters) from the center of the apoptotic cells. (**H**) Time-lapse observation of the rachis bridges outlined with the NMY-2::GFP reporter, (**I**) the apical plasma membranes labeled with the mCherry::PLCΔ^{PH} reporter, and (**J**) the corresponding DIC images in wild-type. For each channel, a single z-section is shown. The yellow arrows point to a cell undergoing apoptosis. The yellow dashed circles in (**H**) outline the rachis bridge of the apoptotic cell. (**K**) Mean area ±SEM of the rachis bridges and the apical plasma membrane in apoptotic cells (magenta lines) and their left and right neighbors (black line), plotted against the relative time before corpse formation. A mean rachis bridge area of 0 indicates full constriction. In each graph, the numbers in brackets refer to the total number of cells analyzed. The scale bars are 10 µm.

166 **CED-3 is necessary for the formation of small germ cell size**

167 To investigate the influence of the CED pathway (Cell Death abnormal) on germ cell size, we
168 tracked germ cells in apoptosis-deficient *ced-3(n717lf) caspase* mutants [35] using the same
169 approach as for the wild-type (**Fig. 1B**). Data for 176 germ cells tracked in three animals
170 indicated that no germ cells that were consistently smaller than their neighbors were present in
171 the pachytene region of *ced-3* loss-of-function (*lf*) mutants (**suppl. Movie S2**). Cell size
172 measurements (**suppl. Fig. S1C**) confirmed the loss of the small cell population (basal cell area
173 below 20 µm^2) in *ced-3(lf)* mutants, especially in the mid to late pachytene region (50-100 µm
174 from the loop), where most apoptotic cell death occurs in the wild-type (**Fig. 2A, B** and **suppl.**
175 **Fig. S2A, B**).
176 We further examined the localization of actomyosin network components in apoptotic corpses
177 using endogenous reporters for the RHO Guanine Exchange Factor (GEF) ECT-2 and the RHO
178 kinase LET-502, along with the non-muscle myosin NMY-2 marker and a germline-specific
179 LifeAct F-actin reporter. All these actomyosin pathway components were strongly enriched at
180 the cortex of dying cells (**Fig. 2C-F'**). Possibly, the overall size reduction of dying cells may
181 have contributed to the compaction of the actomyosin network.
182 Taken together, these data suggest that the full activation of the CED pathway in pachytene
183 stage germ cells is necessary for the formation of small germ cells (<20 µm^2 basal surface) that
184 undergo apoptosis. Dying germ cells exhibit an enhanced accumulation of actomyosin
185 regulators at their cortex, which causes them to fully constrict and cellularize.
186

Figure 2

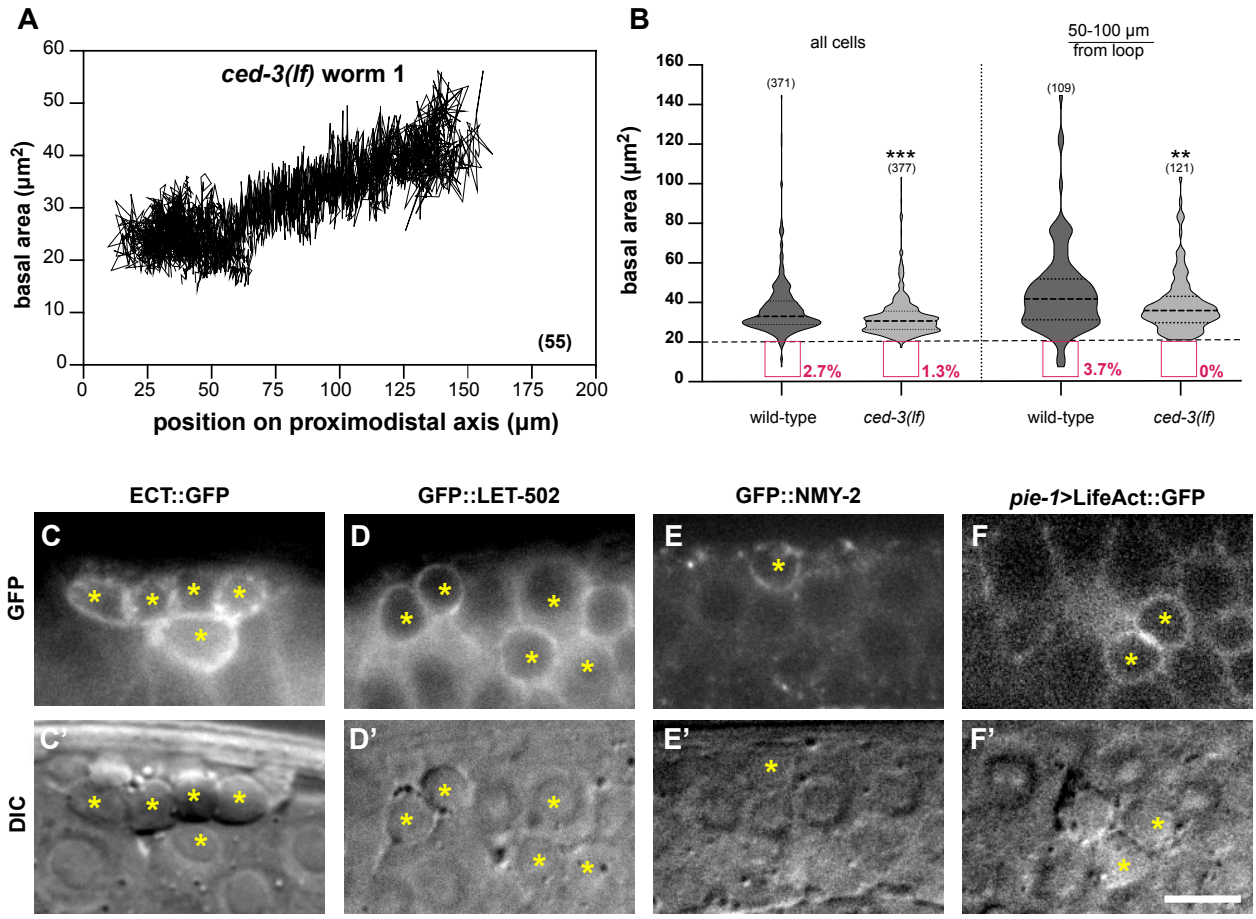

Figure 2. CED-3 Caspase reduces germ cell size.

(**A**) Basal areas of all cells tracked in a *ced-3(lf)* mutant plotted against their relative positions along the distal to proximal axis. Note the absence of small germ cells observed in the wild-type traces in **Fig. 1F**. See **suppl. Fig. S2A, B** for the traces of two additional *ced-3(lf)* animals. (**B**) Violin plots of the basal cell area measured in one-day-old wild-type and *ced-3(lf)* mutants (8 animals each) in the 0-150 µm region (left) or the mid to late pachytene region (right). The red boxes outline the small cells (area < 20 µm^2) and their frequencies. (**C**) Cortical enrichment of the endogenous ECT-2::GFP, (**D**) GFP::LET-502 and (**E**) NMY-2::GFP reporter signals, and (**F**) a germline-specific transgenic *pie-1*>lifeAct::GFP F-actin marker around apoptotic corpses in one-day-old adults. The bottom panels (**C'-F'**) show the corresponding DIC images and the yellow asterisks indicate apoptotic cell corpses. Dashed lines in the violin plots indicate the median values and the dotted lines the upper and lower quartiles. The numbers in brackets in each graph refer to the total number of cells analyzed. Statistical significances were calculated with unpaired two-tailed t-tests (**suppl. Tab. S1**). ** indicates $p < 0.01$ and *** for $p < 0.001$. Scale bar in (**F'**) is 10 µm.

Actomyosin-mediated apical constriction promotes germ cell death

In many cases, programmed cell death is accompanied by a loss of cell volume [36]. However, it is not known if apoptotic signals are the cause of cell shrinkage, or if a reduction in cell size can also trigger the activation of pro-apoptotic pathways. Since we found that germ cells undergo apical constriction and reduce in size before forming apoptotic corpses and since apoptotic corpses are enriched in actomyosin regulators, we tested if altering actomyosin contractility in the germline affects the rate of physiological germ cell death.

We first examined if an increase in actomyosin contractility is sufficient to reduce germ cell size and promote germ cell death. To test this, we used a gain-of-function (*gf*) mutation in *ect-2(zh8gf)*, which encodes a guanine-nucleotide exchange factor that activates the RHO-1 small GTPase [23], combined either with the SYN-4::GFP membrane marker to observe germ cell size or with a CED-1::GFP reporter to score germ cell apoptosis [14,37]. CED-1 is a type 1 trans-membrane receptor expressed in the sheath cells of the somatic gonad that recognizes and clusters around dying cells before they are engulfed [38]. *ect-2(gf)* mutants contained a large number of very small germ cells from the mid to late pachytene region onwards (magenta dots in **Fig. 3B**), interspersed with a few large cells (blue dots) as well as regions devoid of nuclei (green arrowheads, see **suppl. Fig. S3C, D** for full gonad views). Furthermore, many small germ cells were found in the central rachis region, which normally contains only cytoplasm (yellow dots in the mid-sagittal layer and the yz-views in **Fig. 3B)**.

We next tested if the formation of small germ cells in *ect-2(gf)* mutants requires *ced-3 caspase* activity. Small germ cells continued to accumulate in *ect-2(gf); ced-3(lf)* double mutants, indicating that *ect-2* controls germ cell size independently of the CED-pathway (**Fig. 3C** and **suppl. Fig. S3E, F**). Interestingly, both in *ect-2(gf)* single and *ect-2(gf); ced-3(lf)* double mutants small germ cells were only present from the mid to late pachytene region on towards the proximal region (**suppl. Fig. S3C-F**). Thus, activation of the ECT/RHO/ROCK pathway alone is not sufficient to reduce germ cell size in more distal regions, as apical constriction may depend on another signal received by germ cells progressing through pachytene.

ect-2(gf) mutants exhibited a strong increase in the number of apoptotic germ cells detected by the CED-1::GFP reporter (**Fig. 3D**). To determine if the elevated number of apoptotic germ cells in *ect-2(gf)* mutants was due to DNA damage-induced or physiological cell death, we introduced a loss-of-function (*lf*) mutation in the p53 homolog *cep-1* [39]. *cep-1(gk138lf)* mutants do not show an increase in germ cell death after DNA damage, while physiological germ cell death occurs normally [30]. *ect-2(gf)*; *cep-1(lf)* double mutants exhibited a significant

increase in the number of apoptotic germ cells compared to *cep-1(lf)* single mutants and only a slight reduction relative to *ect-2(gf)* single mutants (**Fig. 3D**). Besides inducing actomyosin contractility, ECT-2 also regulates the disassembly of the synaptonemal complexes in pachytene stage germ cells [40]. Therefore, the increased germ cell death observed after hyper-activation of ECT-2 could be due to chromosome pairing defects. To test this possibility, we examined the effect of a *lf* mutation in *pch-2*, which encodes a component of a meiotic checkpoint that activates apoptosis if un-synapsed chromosomes are detected [41]. *ect-2(gf) pch-2(tm1458)* mutants showed a significant increase in germ cell death compared to *pch-2(tm1458)* single mutant and no decrease relative to *ect-2(gf)* single mutants (**suppl. Fig. S3G**). By contrast, very few apoptotic corpses were detected in *ect-2(gf); ced-3(lf)* double mutants (**suppl. Fig. S3H**). Thus, the increased number of apoptotic corpses observed in *ect-2(gf)* mutants is predominantly caused by enhanced physiological germ cell death.

We then reduced the activities of different actomyosin regulators and scored germ cell death as well as apical germ cell constriction by measuring the size of the apical NMY-2::GFP rings on the rachis bridges. Global RNAi against the RHO-dependent kinase *let-502 rock* [24,25] from the L1 stage onwards increased the sizes of the rachis bridges in pachytene stage germ cells, as reported previously [19], without perturbing the cellular integrity as examined with the mCherry::PLCΔ^{PH} plasma membrane marker (**Fig. 3E-G,** see **suppl. Fig. S3I** and **Extended Methods** for the quantification of rachis bridge areas). By contrast, constitutive RNAi against the *rho gef ect-2* or the non-muscle myosin *nmy-2* caused a severe disruption of gonad morphology such that the apical actomyosin corset and lateral germ cell membranes collapsed, precluding the quantification of germ cell death and apical constriction.

We therefore performed germline-specific RNAi, using a strain expressing the Argonaute protein RDE-1 exclusively in the germ cells [42] and the CED-1::GFP marker to score germ cell death. Germline-specific RNAi against *nmy-2*, *ect-2* or *let-502* from the L4 stage decreased the number of CED-1::GFP positive cells in one-day-old adults when compared to empty vector-treated control animals (**Fig. 3H**). It should be noted that the stronger decrease in CED-1::GFP positive germ cells after *ect-2* RNAi, but not *nmy-2* or *let-502* RNAi, may in part be due to the collapse of the plasma membranes since the gonad architecture appeared disorganized and clumps of nuclei formed in around 70% of *ect-2* RNAi treated animals. Also, a transient 4-hour-long inactivation of NMY-2 using the temperature-sensitive *nmy-2(ne1490ts)* allele [43] caused a reduction in the number of CED-1::GFP positive cells at the restrictive temperature (**Fig. 3I**).

Taken together, these data indicate that a decrease in actomyosin contractility increases the size of the apical rachis bridges and reduces germ cell apoptosis, while hyper-activation of the ECT/RHO/ROCK pathway is sufficient to increase the rate of germ cell apoptosis. Thus, apical germ cell constriction promotes physiological germ cell death.

Figure 3

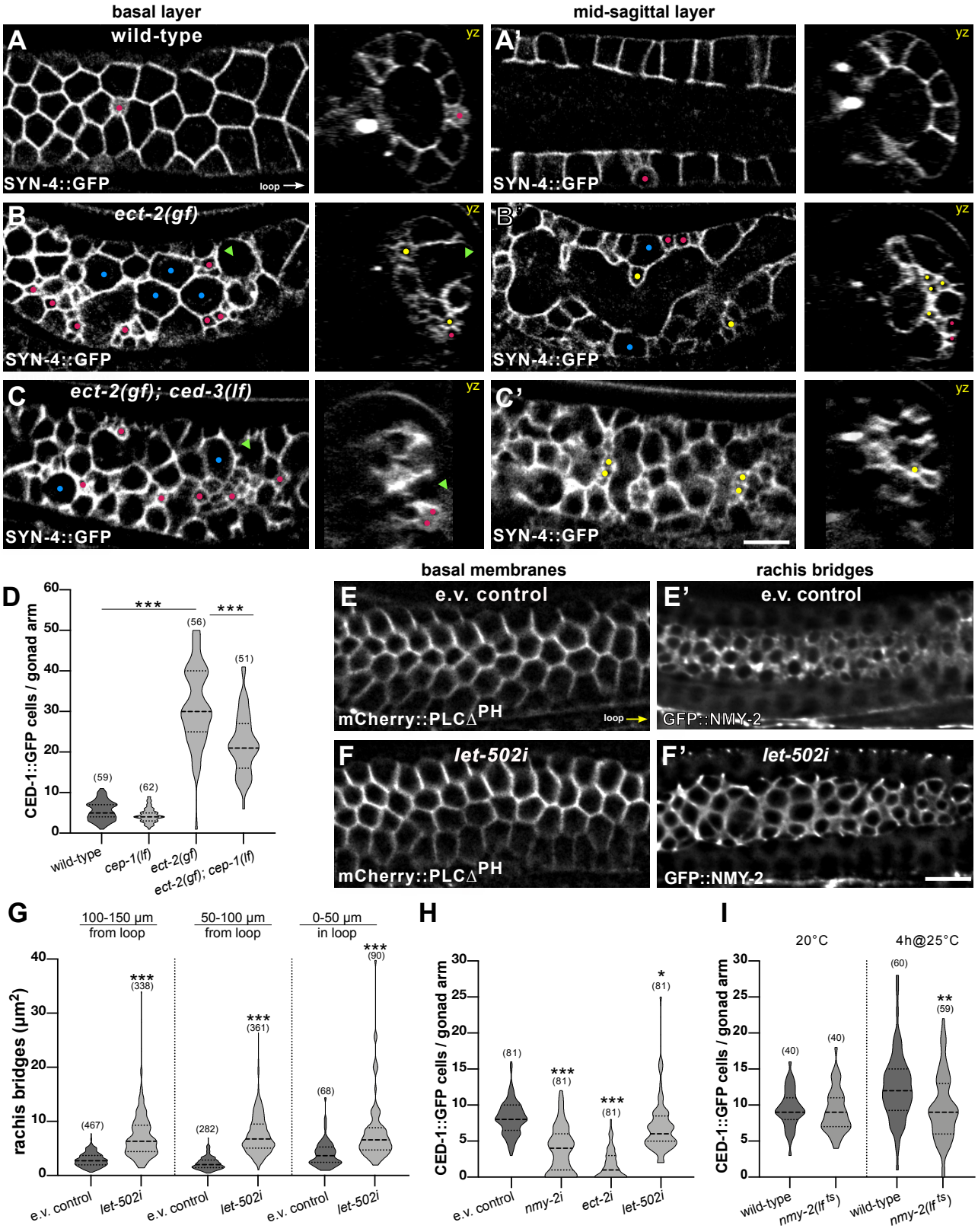

Figure 3. Actomyosin-mediated apical constriction promotes germ cell death.
Germ cell shapes visualized with the SYN-4::GFP plasma membrane marker in (**A**) wild-type, (**B**) *ect-2(gf)* single and (**C**) *ect-2(gf); ced-3(lf)* double mutants. For each genotype, optical sections of the basal surface (**A-C**) and the mid-sagittal layers (**A'-C'**) are shown along with the corresponding yz-projections. Magenta dots highlight some of the small cells localized on the surface, yellow dots some of the small cells inside the rachis, blue dots some large cells, and green arrowheads regions devoid of cells. (**D**) Violin plot showing the number of CED-1::GFP positive apoptotic germ cells per gonad arm in one-day-old adults of the indicated genotypes. (**E**) Basal germ cell surfaces visualized with the mCherry::PLCΔ^{PH} membrane marker and (**E'**) the apical rachis bridges outlined with the NMY-2::GFP marker in animals treated with the empty vector (e.v.) as negative control and (**F, F'**) after global *let-502 rock* RNAi from the L1 stage on until adulthood. (**G**) Violin plot showing the size of the rachis bridges in the three indicated gonad regions in empty vector controls and after global *let-502* RNAi for 72 hours in one-day-old adults, quantified as illustrated in **suppl. Fig. S3H**. Twelve animals were analyzed for e.v. controls and 13 animals for *let-502i*. (**H**) CED-1::GFP positive apoptotic germ cells per gonad arm in one-day-old adults after germline-specific RNAi of the indicated genes. Animals were exposed to dsRNA-producing bacteria from the L4 stage for 24 hours. (**I**) CED-1::GFP positive cells per gonad arm in one-day-old wild-type and temperature-sensitive *nmy-2(lf^{ts})* mutants at the permissive temperature (20°C, left) and after a 4-hour up-shift to the restrictive temperature (4h@25°C, right). Dashed lines in the violin plots indicate the median values and the dotted lines the upper and lower quartiles. For the rachis bridges, the numbers in brackets refer to the number of cells analyzed, and for the CED-1::GFP reporter, the number of animals scored. Statistical analysis was done by one-way ANOVA followed by a Tukey's test for multiple comparisons for **Fig. 3D, H, I** or with an unpaired two-tailed t-test for **Fig. 3G** (**suppl. Tab. S1**). * indicates $p < 0.05$, ** $p < 0.01$ and *** $p < 0.001$. Scale bars are 10 µm.

RAS/MAPK signaling promotes physiological germ cell death

Previous studies have shown that the RAS/MAPK pathway is an essential regulator of physiological and damage-induced germ cell death [11,30,44]. An increase in MAPK activity at the late pachytene stage results in the formation of more but smaller oocytes and an elevated number of apoptotic corpses, while reduced MAPK activity delays pachytene exit and reduces the number of oocytes in the proximal gonads [11,45–48]. The consequences of reducing MAPK activity on germ cell apoptosis are controversial. Some studies observed reduced apoptosis [11,30,45], while Das et al. [48] reported increased apoptosis after inhibition of the MAP kinase MPK-1 using the temperature-sensitive *mpk-1(ga111)* allele [49].

Consistent with the previous reports, we observed an elevated number of CED-1::GFP positive germ cells after transient hyper-activation of the RAS/MAPK pathway by growing temperature-sensitive *let-60 ras(ga89^{ts})* gain-of-function mutants [50] (abbreviated *let-60 ras(gf^{ts})*) for 4 hours at the restrictive temperature of 25°C (**Fig. 4A**). The increase in germ cell apoptosis was independent of *cep-1* and *pch-2*, indicating that elevated RAS/MAPK signaling stimulates physiological germ cell death, rather than activating a DNA damage response or meiotic checkpoint (**Fig. 4A, suppl. Fig. S4B**). On the other hand, germ cell death in *let-60 ras(gf^{ts})* mutants completely depended on *ced-4* activity (**suppl. Fig. S4A**), indicating that RAS/MAPK signaling promotes germ cell death via the canonical CED pathway [7,11].

To score germ cell death after reduced RAS/MAPK signaling in the germline, we first performed germline-specific RNAi knock-down of the MAPK *mpk-1* and observed a slight reduction in the number of CED-1::GFP positive germ cells (**Fig. 4B**). By contrast, global reduction of MPK-1 activity in the soma and the germline using the temperature-sensitive *mpk-1(ga111 ^{ts})* reduction-of-function allele [49] (abbreviated *mpk-1(lf ^{ts})*) did not result in a significant change in the number of CED-1::GFP positive germ cells (**Fig. 4B**). However, a strain carrying the *mpk-1(lf^{ts})* allele and simultaneously expressing the somatic *mpk-1a* isoform from an extrachromosomal array exhibited a significantly reduced number of CED-1::GFP positive germ cells at the restrictive temperature (**Fig. 4B** and **suppl. Fig. S4C**). Possibly, the somatic *mpk-1a* isoform plays a role in the gonadal sheath cells, for example during the clearing of apoptotic corpses. Hence, if MAPK signaling is simultaneously reduced in the soma and germline, a decrease in germ cell apoptosis may be compensated for by reduced MPK-1A activity in the soma. To further distinguish between the activities of the somatic *mpk-1a* and the germline-specific *mpk-1b* isoforms, we generated the germline-specific *mpk-1b(zh164)* allele (abbreviated *mpk-1b(lf))* by introducing a stop codon in the first exon of the *mpk-1b*

isoform (W4Stop, see **materials and methods**). Germline-specific *mpk-1b(lf)* mutants contained only a few CED-1::GFP positive cells (**Fig. 4B** and **suppl. Fig. S4C**).

Taken together, we propose that the somatic *mpk-1a* isoform may play a role in apoptotic corpse clearing, while the germline-specific *mpk-1b* isoform promotes physiological germ cell death.

Hyper-activation of RAS/MAPK signaling decreases basal germ cell area

Hyperactivation of the RAS/MAPK pathway or enhanced RHO/ROCK signaling both resulted in an elevated rate of physiological germ cell death. These observations raised the possibility that enhancing RAS/MAPK signaling might also cause a reduction in germ cell size, which in turn would promote germ cell death. To test this hypothesis, we first performed RNAi against the non-muscle myosin NMY-2 in the temperature-sensitive *let-60(gf^{ts})* background and observed the CED-1::GFP marker to score germ cell apoptosis and the mCherry::PLCΔ^{PH} membrane marker to assess plasma membrane integrity. RNAi against *nmy-2* was carried out for 24 hours from the L4 stage on, combined with a hyper-activation of *let-60 ras* signaling at 25°C for the last four hours, or with a simultaneous 24-hour-long hyper-activation of *let-60 ras* from the L4 stage on. Both treatments decreased the number of CED-1::GFP positive germ cells (**Fig. 4C** and **suppl. Fig. S4D**). The increase in physiological germ cell death observed after hyper-activation of the RAS/MAPK pathway therefore depends, at least in part, on the activity of the actomyosin network.

We next examined germ cell size by observing the SYN-4::GFP plasma membrane marker in temperature-sensitive *let-60(gf^{ts})* mutants grown for 4 hours at the restrictive temperature. Hyper-activation of the RAS/MAPK pathway resulted in the formation of more small germ cells (basal area below 20 µm^2), especially at the late pachytene stage 50-100 µm before the loop (magenta boxes in **Fig. 4D** and dots in **Fig. 4E, F**). Also, the average size of all germ cells combined was reduced in *let-60(gf^{ts})* mutants (**Fig. 4D** and **suppl. Fig. S4E**).

The effect of the RAS/MAPK pathway on germ cell size may be indirect. For example, RAS/MAPK signaling could directly activate the pro-apoptotic CED pathway, which would cause apoptotic germ cells to shrink. Alternatively, RAS/MAPK signaling may regulate germ cell size through the actomyosin pathway independently of the CED pathway.

To distinguish between these two possibilities, we quantified germ cell sizes in *let-60(gf^{ts}); ced-4(lf)* double mutants, as well as in *ced-4(lf)* single mutants. Small germ cells (basal area below 20 µm^2) accumulated in the pachytene region of *let-60(gf^{ts}); ced-4(lf)* double mutants

mostly inside the rachis (**Fig. 4D, H**), while *ced-4(lf)* single mutants did not contain any small germ cells (**Fig. 4D, G**), similar to *ced-3(lf)* mutants (**Fig. 2A, B**). Since an accurate quantification of germ cells inside the rachis was not possible using our MorphographX pipeline, the fraction of small cells shown in **Fig. 4D** for *let-60(gf^{ts}); ced-4(lf)* double mutants is probably an underestimate, as it only includes small cells at the basal surface. Moreover, in the late pachytene region (50-100 µm before the loop) the average germ cell size in *let-60(gf^{ts}); ced-4(lf)* double mutants was significantly smaller than in *ced-4(lf)* single mutants and more similar to *let-60(gf^{ts})* single mutants, except for the reduced fraction of very small cells (**Fig. 4D** and **suppl. Fig. S4E**).

To directly correlate germ cell size and apoptosis in *let-60(gf^{ts})* mutants, we compared the sizes of CED-1::GFP-positive cells to their CED-1::GFP-negative neighbors in the late pachytene region (50-100 µm) using the mCherry::PLCΔ^{PH} membrane marker (**Fig. 4I** and **Extended Methods**). Small germ cells (basal area below 20 µm^2) were more likely to be CED-1::GFP positive (73%) than larger cells. However, it should be noted that a population of CED-1::GFP negative small cells (16%) was also observed. Since the germ cell tracking experiments (**Fig. 1**) indicated that germ cells with a basal area below 20 µm^2 have a 58% probability of forming an apoptotic corpse within one hour, the population of CED-1::GFP-negative small cells may contain pre-apoptotic cells that have not yet been engulfed.

Taken together, our data indicate that RAS/MAPK signaling decreases germ cell size independently of the CED pathway. The smaller germ cells generated in the wild-type or after hyper-activation of the RAS/MAPK pathway are more likely to be engulfed than their larger neighbors.

Figure 4

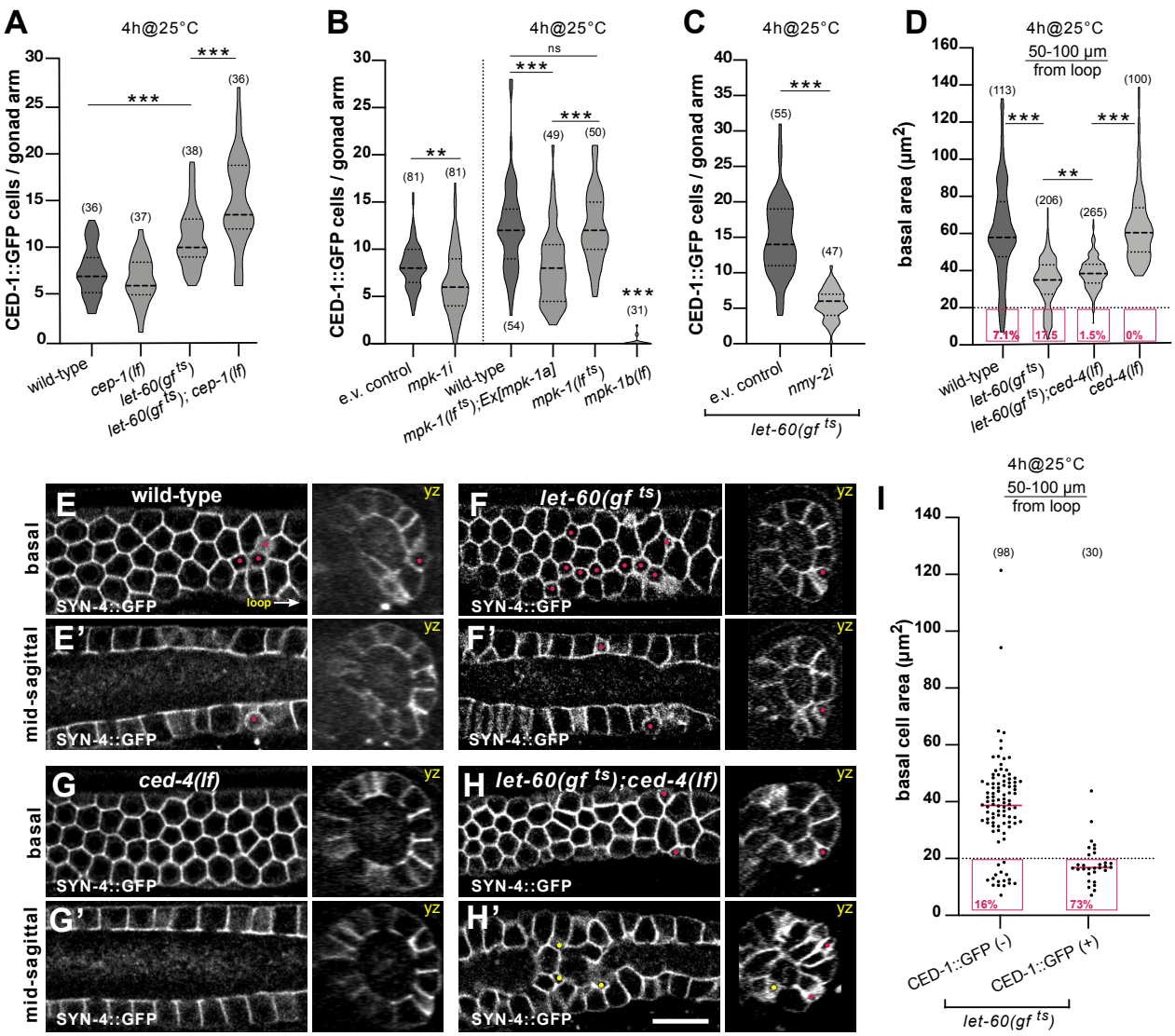

Figure 4. RAS/MAPK signaling promotes apoptosis

(**A**) Violin plot showing the number of CED-1::GFP positive apoptotic germ cells per gonad arm in one-day-old adults of the indicated genotypes grown at 20°C for 68 hours and subsequently up-shift for 4 hours to the restrictive temperature (4h@25°C). (**B**) CED-1::GFP positive apoptotic germ cells in one-day-old adults after germline-specific RNAi of *mpk-1* for 24 hours from the L4 stage on (left) and in wild-type, temperature-sensitive *mpk-1(lf^{ts})* mutants with or without the *Ex[mpk-1a]* transgene expressing the *mpk-1a* isoform in the soma, and the germline-specific *mpk-1b(lf)* allele. Twenty hours post L4 the animals were grown for 4 hours at the restrictive temperature of 25°C (4h@25°C, right side). Controls grown continuously at 20°C are shown in **suppl. Fig. S4C**. (**C**) CED-1::GFP positive apoptotic germ cells in one-day-old adult *let-60(gf^{ts})* mutant treated with empty vector or *nmy-2i*. Animals were RNAi treated for 24 hours from the L4 stage on and up-shifted to 25°C for the last 4 hours before scoring the corpses (for 24 hours up-shift at 25°C see **Suppl. Fig. S4D**). (**D**) Violin plot of the basal cell areas in the late pachytene region (50-100 µm from the loop) measured using MorphographX in one-day-old adults of the indicated genotypes. Twenty hours post L4 the animals were grown

for 4 hours at the restrictive temperature of 25°C (4h@25°C). The magenta boxes outline the small cells (area < 20 µm^2) and their frequencies are shown as percentage values. Results of the size measurements in the other gonad regions are shown in **suppl. Fig. S4E**. Ten animals were analyzed for wild-type, 15 animals for *let-60(gf^{ts}),* 16 animals for *let-60(gf^{ts}); ced-4(lf)* and 9 animals for *ced-4(lf)*. (**E**) Germ cell shapes visualized with the SYN-4::GFP plasma membrane markers in wild-type, (**F**) in *let-60(gf^{ts})*, (**G**) *ced-4(lf)* single, and in (**H**) *let-60(gf^{ts}); ced-4(lf)* double mutant. For each genotype, optical sections of the basal surface (**E-H**) and the mid-sagittal layers (**E'-H'**) are shown along with the corresponding yz-projections. Magenta dots highlight small cells localized on the surface and yellow dots small cells inside the rachis. (**I**) Basal cell areas in the late pachytene region (50-100 µm region) of CED-1::GFP negative cells versus CED-1::GFP positive cells in one-day-old adults of *let-60(gf^{ts})* grown at 20°C for 68 hours and incubated for 4 hours at the restrictive temperature of 25°C. Fifteen *let-60(gf^{ts})* animals were analyzed. Dashed lines in the violin plots indicate the median values and the dotted lines the upper and lower quartiles. For the measurements of the basal areas, the numbers in brackets refer to the numbers of cells analyzed, and for the CED-1::GFP reporter to the numbers of animals scored. Statistical analysis was done using one-way ANOVA followed by a Tukey's test for multiple comparisons or with an unpaired two-tailed t-test (**suppl. Tab. S1**). ** indicates $p < 0.01$ and *** $p < 0.001$ Scale bars are 10 µm.

RAS/MAPK signaling induces apical germ cell constriction

We have previously reported that activation of the RAS/MAPK pathway by the EGF receptor induces apical constriction of the primary vulval precursor cells during morphogenesis of the hermaphrodite vulva [51]. This finding raised the possibility that RAS/MAPK signaling could also induce apical constriction at the rachis bridges of germ cells in the pachytene region to regulate germ cell size and death.

To investigate this hypothesis, we measured the sizes of the rachis bridges after hyper-activation or inhibition of RAS/MAPK signaling, by combining the temperature-sensitive *let-60(gf^{ts})* and *mpk-1(lf^{ts})* alleles with the endogenous NMY-2::GFP non-muscle myosin marker, which outlines the rachis bridges (**Fig. 5A**). In one-day-old adult *let-60(gf^{ts})* animals grown for 4 hours at the restrictive temperature, the average area of the rachis bridges was decreased (**Fig. 5A-C**) and **suppl. Fig. S5A, B**). In many cases, the NMY-2::GFP signal accumulated in single bright spots, which could not be quantified, on the apical side facing the rachis (yellow arrows in **suppl. Fig. S5A, B**), suggesting that the apical rachis bridges in those cells had already fully constricted. Conversely, in young adult *mpk-1(lf^{ts})* animals grown for 4 or 6 hours at the restrictive temperature, the average area of the rachis bridges was increased (**Fig. 5D-F** and **suppl. Fig. S5C-E**).

To study the effects of altered RAS/MAPK signaling on gonad architecture, we compared the heights of the germ cells as well as the rachis diameter in the pachytene region (50 to 150 µm from the loop) of wild-type, *let-60(gf^{ts})* and *mpk-1(lf^{ts})* mutants. To measure the average rachis diameters, the total areas of the regions shown in **Fig. 5J'-L'** were measured in mid-sagittal sections and divided by their length (100µm). In one-day-old *let-60(gf^{ts})* mutants incubated for 4 hours at 25°C, the average rachis diameter was decreased by 39%, while the average height of the cells was increased by 6.6% relative to the wild-type. Conversely, in *mpk-1(ts lf)* mutants incubated at 25°C for 4 hours the average rachis area was expanded by 21%, while the average height of the cells was decreased by 8.6%. (**Fig. 5G-I**).

Together these results suggest that RAS/MAPK signaling promotes actomyosin constriction at the apical rachis bridges. In addition, elevated RAS/MAPK signaling results in a decreased diameter of the central rachis and elongation of the pachytene germ cells along their apicobasal axis.

Figure 5

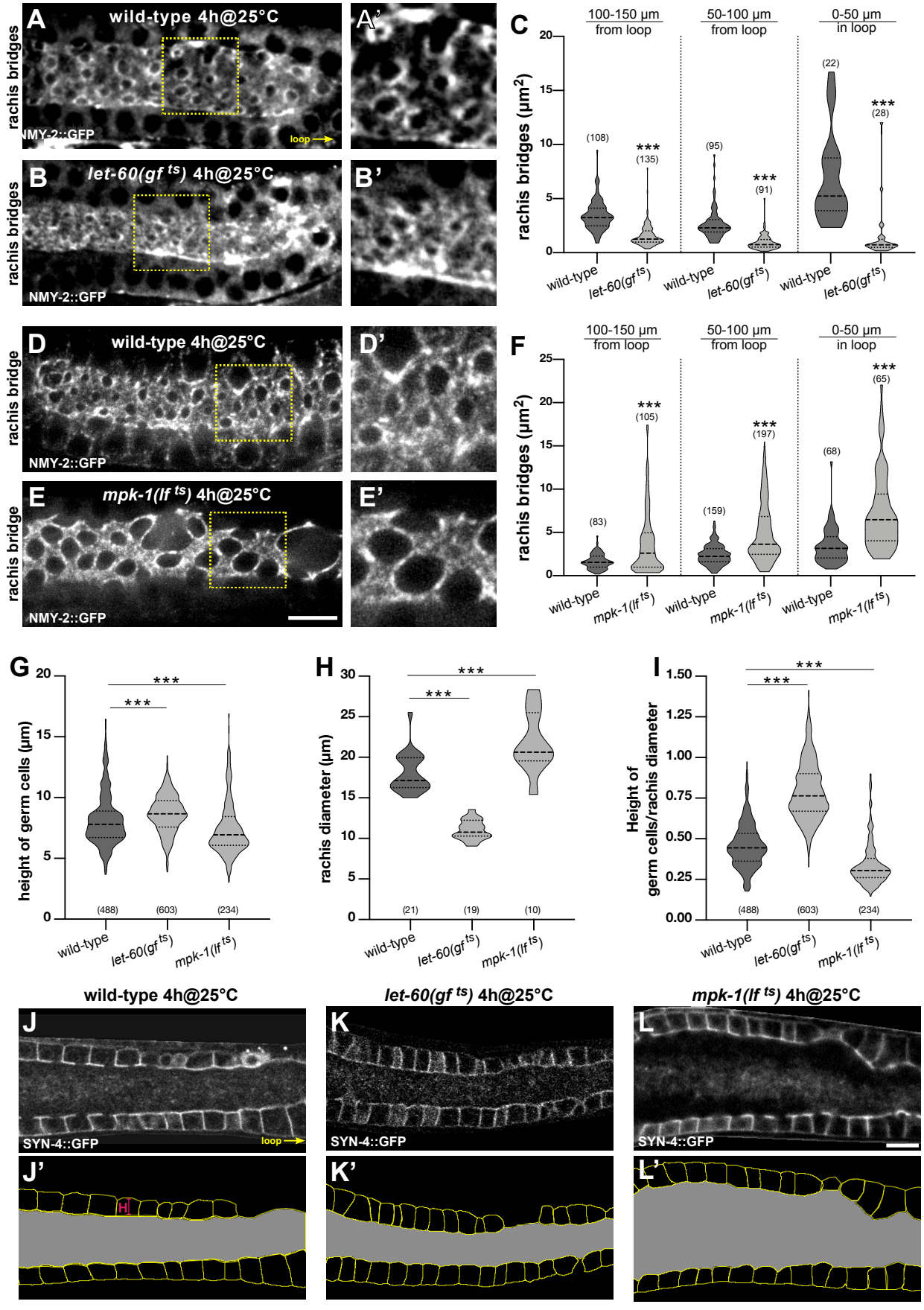

453

Figure 5. RAS/MAPK signaling promotes apical germ cell constriction

(**A, B**) Rachis bridges outlined by the NMY-2::GFP reporter in one-day-old wild-type and *let-60(gf^{ts})* mutant animals grown for 4 hours at the restrictive temperature of 25°C. (**A'**) and (**B'**) show two-fold magnifications of the regions outlined by the dashed yellow boxes in (**A**) and (**B**). Additional examples of the rachis bridges in wild-type and *let-60(gf^{ts})* mutants are shown in **suppl. Fig. S5A-B**. (**C**) Violin plots showing the size of the rachis bridges in wild-type and *let-60(gf^{ts})* mutant animals in the three indicated gonad regions. Five animals were analyzed for wild-type and 6 animals for *let-60(gf^{ts})*. (**D, E**) Rachis bridges in wild-type and *mpk-1(lf^{ts})* mutant animals grown for 4 hours at the restrictive temperature (4h@25°C) at the L4 stage. (**D'**) and (**E'**) show two-fold magnifications of the regions outlined by the dashed yellow boxes in (**D**) and (**E**). (**F**) Violin plots showing the size of the rachis bridges in wild-type and *mpk-1(lf^{ts})* mutant animals in the three indicated gonad regions. Nine animals were analyzed for wild-type and 8 animals for *mpk-1(gf^{ts})*. The quantification of the rachis bridges after a 6-hour inactivation of MPK-1 is shown in **suppl. Fig. S5C-E**. (**G**) Violin plots showing the height of pachytene germ cells (lateral membranes 50 to 150 µm from the loop) in wild-type, *let-60(gf^{ts})* and *mpk-1(lf^{ts})* mutants, grown at 20°C for 68 hours and incubated for the last 4 hours at 25°C. Twenty-one animals were analyzed for wild-type, 19 for *let-60(gf^{ts})* and 10 for *mpk-1(lf^{ts})*. (**H**) Violin plots show the average diameter of the rachis in the same animals as in (**G**). (**I**) Violin plots showing the ratios of germ cell height to rachis diameter. (**J-L**) Mid-sagittal sections of a wild-type, a *let-60(gf^{ts})* and an *mpk-1(lf^{ts})* mutant were used to measure cell height and rachis diameter shown in (**G-I**). (**J'-L'**) Masks generated from the animals shown in (**J-L**) using the cellpose algorithm [52]. Cell borders are shown in yellow and the rachis area is in grey. Dashed lines in the violin plots indicate the median values and the dotted lines the upper and lower quartiles. For the measurements of the rachis bridges and cell heights, the numbers in brackets refer to the number of cells analyzed, and for the rachis diameter to the number of animals scored. Statistical analysis was done using one-way ANOVA followed by a Tukey's test for multiple comparisons or with an unpaired two-tailed t-test (**suppl. Tab. S1**). ** indicates $p < 0.01$ and *** $p < 0.001$ Scale bars are 10 µm.

RAS/MAPK signaling is necessary for NMY-2 myosin enrichment at the rachis bridges

To investigate the interactions between the ECT/RHO/ROCK and RAS/MAPK pathways, we combined the germline-specific *mpk-1b(lf)* or the temperature-sensitive *mpk-1(lf^{ts})* alleles with the *ect-2(gf)* mutation and scored germ cell apoptosis using the CED-1::GFP marker. The germline-specific *mpk-1b(lf)* allele in particular excludes possible interference caused by loss of the somatic MPK-1A isoform. Animals were scored 24 hours after the L4 stage at 20°C or for the *mpk-1(lf^{ts})* allele after incubation at 25°C for the final 4 hours. *ect-2(gf); mpk-1b(lf)* double mutants displayed a strong reduction in CED-1::GFP positive cells compared to *ect-2(gf)* single mutants (**Fig. 6A**, left). Also in *ect-2(gf); mpk-1(lf^{ts})* double mutants, the number of CED-1::GFP positive cells decreased to the level of *mpk-1(lf^{ts})* single mutants (**Fig. 6A**, right). Therefore, MPK-1 acts either downstream of ECT-2, or RAS/MAPK signaling promotes germ cell death in parallel with the ECT/RHO/ROCK pathway through a different mechanism.

To examine if MAPK activity is regulated by the ECT/RHO/ROCK pathway, we quantified the levels of the activated, di-phosphorylated 50.6 kD MPK-1B isoform (P-MPK-1B) by Western blot analysis using a di-phospho-specific ERK antibody [47]. Analysis of whole-animal extracts of 1 day-old adult *ect-2(gf)* and *let-502(lf^{ts})* animals grown for 4 hours at the restrictive temperature of 25°C revealed no significant changes in P-MPK-1B levels (**Fig. 6B** and **suppl. Fig. S6A-A''**). Thus, the RAS/MAPK and ECT/RHO/ROCK signaling pathways likely act through distinct mechanisms to induce apical germ cell constriction and death.

To investigate how RAS/MAPK signaling controls germ cell constriction, we examined the sub-cellular distribution of NMY-2::GFP myosin. In the late pachytene region (50-100µm from the loop) of one-day-old adult wild-type animals, NMY-2::GFP was enriched in punctate structures around the rachis bridges (**Fig. 6C**, see **suppl. Fig. S6B** for intensity profiles and additional examples). In *mpk-1b(lf)* mutants, on the other hand, NMY-2::GFP enrichment at the rachis bridges was reduced, and the NMY-2::GFP puncta were evenly distributed on the apical cortex between the rachis bridges (**Fig. 6D** and **suppl. Fig. S6C**). Since the diameter of the rachis bridges was enlarged in *mpk-1b(lf)* mutants and hence the area of the apical cortex between the rachis bridges reduced, *mpk-1b(lf)* likely resulted in a higher local NMY-2::GFP concentration on the apical cortex. Quantification of the average NMY-2::GFP intensities over the entire apical surface including the rachis bridges indicated that loss of *mpk-1b* did not significantly alter total NMY-2::GFP levels (**suppl. Fig. S6D, D'**). Reduced NMY-2::GFP

localization at the rachis bridges was also observed in *mpk-1(lf^{ts})* mutants, though the effect was less pronounced due to the partial inactivation of *mpk-1* (**Fig. 5E** and **suppl. Fig. S5D**). Thus, RAS/MAPK signaling may be necessary to localize NMY-2 to the rachis bridges. However, it should be noted that the lower levels of NMY-2::GFP at the rachis bridges could also be an indirect consequence of the changed gonad morphology (i.e. the enlarged rachis bridges) in *mpk-1(lf)* mutants.

To test if the altered distribution of NMY-2 in *mpk-1b(lf)* and *mpk-1(lf^{ts})* mutants changed actomyosin contractility, we performed laser ablation experiments to measure the cortical tension, as described [18,53]. Using a pulsed UV-laser, we created point incisions on the apical membranes between the rachis bridges, followed the expansion of the incisions by tracking the displacement of individual NMY-2::GFP foci (**Fig. 6E, F** and **suppl. Fig. S6E**), and quantified the initial recoil velocity and total recoil as indicators of the cortical tension [53] (see also materials and methods). The initial recoil velocity and the total recoil were both increased in *mpk-1b(lf)* mutants grown at 20° (**Fig. 6G, H)** and in *mpk-1(lf^{ts})* mutants grown for 4 hours at 25°C (**suppl. Fig. S6F, G**). On the other hand, RNAi of *let-502 rock* resulted in a smaller total recoil, though the initial recoil velocity was not significantly changed (**Fig. 6F-H**).

We conclude that RAS/MAPK signaling is not necessary to induce actomyosin contractility, but rather to control the sub-cellular distribution of NMY-2 myosin. The increased recoil in *mpk-1* mutants may be due to the changed NMY-2 localization, resulting in a higher local concentration of NMY-2 on the apical cortex. Inhibition of *let-502 rock*, on the other hand, causes a global reduction of actomyosin contractility and a reduced tension on the apical cortex.

Figure 6

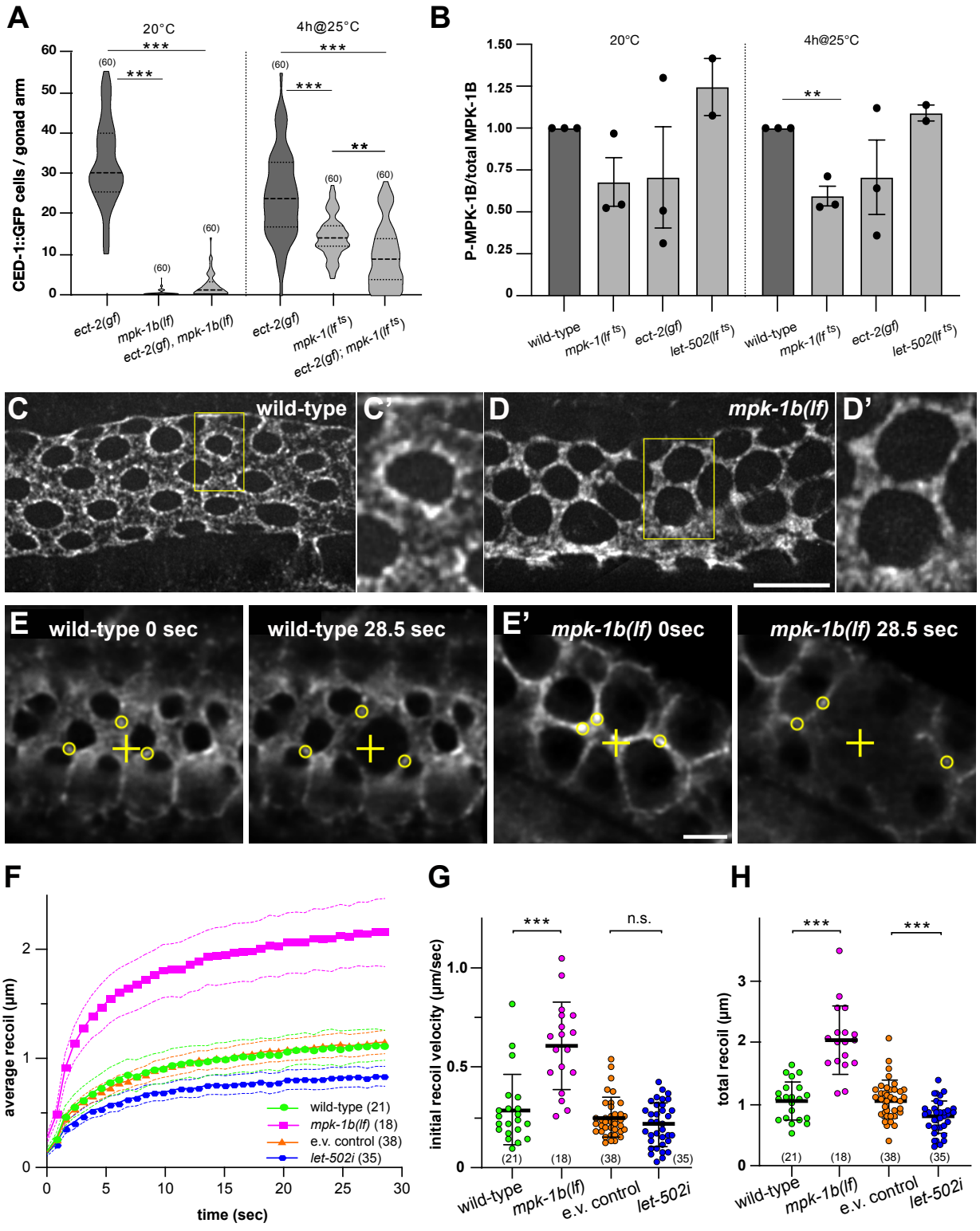

Figure 6. RAS/MAPK signaling controls NMY-2 myosin localization at the rachis bridges

(**A**) Violin plot showing the number of CED-1::GFP positive apoptotic germ cells per gonad arm in one-day-old adults of the indicated genotypes, grown either at 20°C (left) or up-shifted to 25°C for the last 4 hours (right). (**B**) Quantification of di-phosphorylated MPK-1B (P-MPK-1B) and total MPK-1B protein levels on Western blots of total extracts from one-day-old adults

of the indicated genotypes, incubated either at 20°C or for the final 4 hours at 25°C. The average intensity ratios ± SEM of the P-MPK-1B to MPK-1B signals, each normalized to the tubulin loading controls and relative to the wild-type control values obtained in each experiment are shown. Quantification of three biological replicates as described in Materials and Methods, except for two *let-502* replicates. Individual blots are shown in **suppl. Fig. S6A-A''**. (**C**) NMY-2::GFP localization in wild-type and (**D**) *mpk-1b(lf)* mutants in the late pachytene region (50-100µm from the loop) 66 to 68 hours post-L1 arrest. Maximum intensity projections of deconvolved z-stacks spanning the apical surface are shown. The yellow boxes outline the regions shown at two-fold magnification in (**C'**) and (**D'**). NMY-2::GFP intensity profiles across the rachis bridges and additional examples are shown in **suppl. Fig. S6B, C**. (**E**) Recoil after point incision in wild-type and (**E'**) *mpk-1b(lf)* one-day-old adults (66 to 68 hours after L1 arrest). The left frames (0 sec) show the apical surface before and the right frames 28.5 sec after the incision. The yellow crosses indicate the incision point and the circles mark NMY-2::GFP foci used to track the mean radial displacement from the incision points. See **Movies S3 & S4** for all time points of the examples shown, and **suppl. Tab. S1** for the individual measurements of all animals scored. (**F**) Mean radial displacement (recoil) plotted against time after incision. The symbols indicate the average recoil of all animals analyzed and the dashed lines the 95% CI. (**G**) Initial recoil velocities and (**H**) total recoil in the indicated genotypes/ conditions were calculated for each animal individually. See materials and methods for details on the curve fitting and quantification. Dashed horizontal lines in the violin plots in (**A**) indicate the median values and dotted lines the upper and lower quartiles, solid horizontal lines in (**G**) and (**H**) the mean values ± SD. The numbers in brackets refer to the numbers of animals analyzed. Statistical analysis was done using one-way ANOVA followed by a Tukey's test for multiple comparisons (**A, B**) or by unpaired t-tests (**G, H**) (**suppl. Tab. S1**). ** indicates $p < 0.01$ and *** $p < 0.001$. Scale bars in (**D**) and (**E'**) are 10µm and 5µm, respectively.

Discussion

Apoptotic cell death is a ubiquitous process that serves to maintain cellular homeostasis in self-renewing organs [2–4]. We have investigated germ cell apoptosis in *C. elegans* hermaphrodites, a physiological process that eliminates around 60% of all germ cells during the pachytene stage of meiotic prophase I. In contrast to the programmed cell death occurring during embryo and larval development in the *C. elegans* soma, physiological germ cell death in adult animals appears to be a stochastic process that eliminates randomly selected cells.

Here, we show that pachytene stage germ cells smaller than their neighbors are selectively eliminated through apoptosis, probably to make space for and donate their resources to the surviving germ cells entering oogenesis [11,15]. Apical actomyosin constriction at the rachis bridges that connect the cells to a common cytoplasmic reservoir (the rachis) is jointly controlled by the RAS/MAPK and ECT/RHO/ROCK signaling pathways. Enhancing apical germ cell constriction reduces germ cell size and thereby increases the rate of physiological germ cell death (**Fig. 7**).

The RHO/ROCK pathway promotes physiological germ cell death via apical germ cell constriction

Based on our germ cell tracking data, which demonstrate that germ cells reduce their size 1 to 2 hours before forming apoptotic corpses, we investigated the involvement of the RHO/ROCK pathway in physiological germ cell death. Reducing germ cell size by hyper-activation of the RHO GEF ECT-2 was sufficient to increase germ cell death at the pachytene stage, whereas inhibiting the RHO pathway specifically in germ cells caused a reduction in physiological germ cell death. These data indicated that reduced germ cell size could be a cause and not only a consequence of germ cell death. To exclude the possibility that the reduction in germ cell death observed after inhibiting the ECT/RHO/ROCK pathway was an indirect consequence of an overall loss of cellular integrity, we monitored germ cell shape and chose conditions that only transiently inhibited the ECT/RHO/ROCK pathway without perturbing gonad architecture. Under these conditions, we observed a reduction in apoptotic corpse formation while maintaining germ cell integrity.

The changes in germ cell size and death caused by reducing actomyosin contractility are accompanied by the opening of the rachis bridges. This suggests that germ cell size is regulated by the constriction of the rachis bridges, which regulate the flow of cytoplasm between the germ cells and the rachis. Interestingly, the constriction of the rachis bridges and apoptotic

corpse formation only occurred in the mid to late pachytene region, before the surviving germ cells enter the loop region, where they reopen their rachis bridges and grow in size. These observations suggest that germ cells progressing through the pachytene may receive a positional signal that induces apical germ cell constriction. Moreover, the constitutive activation of the ECT/RHO/ROCK pathway through a *gf* mutation in *ect-2* reduced germ cell size only from the mid to late pachytene region onwards. Thus, apical germ cell constriction in the pachytene region may depend on additional signals, which may be transduced by the RAS/MAPK pathway.

RAS/MAPK signaling induces apical germ cell constriction

The RAS/MAPK pathway regulates oogenesis in various organisms, including *C. elegans, Drosophila* and mammals [46,54–56]. In the *C. elegans* hermaphrodite germline, RAS/MAPK signaling plays an essential role at two stages, during pachytene progression and oocyte maturation [57]. The activation of RAS/MAPK signaling by the DAF-2 insulin receptor in germ cells progressing through the pachytene stage is essential for the germ cells to maintain the membrane integrity, exit pachytene, and initiate oocyte differentiation [29,47,58].

Previous reports have shown that RAS/MAPK signaling at the pachytene stage is required for physiological as well as DNA damage-induced germ cell death [11,30]. We have confirmed this for the physiological cell death by inactivation of the germ cell-specific MPK-1b isoform. Moreover, we show that RAS/MAPK signaling reduces germ cell size by inducing apical constriction at the rachis bridges together with the ECT/RHO/ROCK pathway discussed above. The regulation of germ cell size by RAS/MAPK signaling does not require the activation of the pro-apoptotic CED pathway, indicating that the reduced size of the germ cells in *let-60(gf)* mutants is not a consequence of enhanced apoptosis.

We have previously reported an interaction between the ECT/RHO and the RAS/MAPK pathways during vulval fate specification in the hermaphrodite larva, where hyper-activation of RHO-1 signaling through the *ect-2(gf)* mutation promotes 1° fate specification upstream of or in parallel with MPK-1 signaling [23]. Moreover, activation of the EGFR/RAS/MAPK pathway in the 1° vulval precursor cells is necessary for their apical constriction, which initiates the invagination of the vulval epithelium [51].

The redistribution of NMY-2 from the rachis bridges to the apical cortex in the germline of *mpk-1* mutants likely contributes to the expansion of the rachis bridges. Moreover, the increased recoil after laser incision of the apical germ cell cortex in *mpk-1* mutants suggests

633 that RAS/MAPK signaling is not necessary for actomyosin contractility, but rather for the
634 localization of myosin at the rachis bridges. The reduced levels of NMY-2 at the rachis bridges
635 after the inactivation of RAS/MAPK signaling could be an indirect consequence of changes in
636 gonad architecture that affect the size or integrity of the rachis bridges. Alternatively,
637 RAS/MAPK signaling may directly regulate myosin mobility or recruitment to the rachis
638 bridges, for example via phosphorylation of the myosin heavy chain NMY-2, which prevents
639 the assembly of myosin into filaments [59]. Such a mechanism has recently been discovered
640 during somatic cell death, where PIG-1 MELK phosphorylates NMY-2 to cause asymmetrical
641 cell division and apoptosis [60,61].
642 The changes in gonad architecture after hyperactivation or inhibition of the RAS/MAPK
643 pathway (e.g. the enlarged rachis in *mpk-1(lf)* mutants) cannot intuitively be explained by local
644 changes in actomyosin contractility alone, suggesting that RAS/MAPK signaling affects gonad
645 morphology through additional mechanisms. For example, inhibition of RAS/MAPK signaling
646 may increase the hydrostatic pressure in the gonad due to the lack of oocyte maturation and
647 ovulation [57] and thereby enlarge the rachis diameter, while elevated RAS/MAPK signaling
648 may result in a lowered hydrostatic pressure, and consequently a smaller rachis diameter.
649 Taken together, our data suggest that the RAS/MAPK and ECT/RHO/ROCK pathways act
650 through distinct mechanisms to control germ cell size and death. This model is consistent with
651 previous reports showing that the size of the rachis bridges decreases in the pachytene region
652 where the RAS/MAPK pathway is active and again increases in surviving germ cells that enter
653 the loop region [19]. It should be noted, however, that our data do not exclude the possibility
654 that RAS/MAPK signaling also regulates germ cell death independently of germ cell size
655 through an unknown mechanism (dashed arrow in **Fig. 7**).
656
657 **A contractility-based model for physiological germ cell death**
658 We propose that actomyosin contractility of the rachis bridges, regulated by the combined
659 actions of the RAS/MAPK and ECT/RHO/ROCK pathways, enhances the intrinsic disparities
660 in cell size in the syncytial gonad region. Germ cell tracking experiments revealed that
661 stochastic, initially small size differences between individual germ cells are rapidly amplified,
662 as slightly smaller cells progressively shrink, while their neighbors increase in size. This
663 phenomenon can be explained by the Law of Laplace, which is illustrated by an experiment
664 with two corresponding balloons of unequal sizes, where the initially smaller balloon empties
665 into the larger one. Such a model has been proposed by Chartier *et al.* [31], who found that

hydraulic instability in the syncytial germline amplifies stochastic size differences between the germ cells, causing smaller cells to expel their cytoplasm and die. Specifically, the Law of Laplace (T = P * R/2, where T = surface tension; P = internal pressure, R = cell radius) predicts that for a given internal pressure, which should be equal in all syncytial germ cells connected to the rachis, the surface tension will be lower and therefore actomyosin contractility can be more effective in smaller cells. Hence, germ cells that are slightly smaller than their neighbors are prone to shrink and expel their cytoplasm until their rachis bridges are closed. According to this model, increasing the activity of the RAS/MAPK or ECT/RHO/ROCK pathway will enhance actomyosin contractility at the rachis bridges, which will exacerbate this inherent instability and result in even greater cell size discrepancies and an increased rate of germ cell death.

Shrinking germ cells may not only donate their cytoplasm to the survivors but also lose survival factors that prevent the activation of the CED-3 caspase. Pre-apoptotic germ cells rapidly expel most of their mitochondria [32], which carry anti-apoptotic factors such as the BCL-2 homolog CED-9 [62]. However, a *ced-9(gf)* mutation only slightly affects physiological germ cell death, suggesting that germ cells contain additional anti-apoptotic factors. In mutants blocking mitochondrial expulsion, the germ cells can still undergo apoptosis [32], suggesting that anti-apoptotic factors localized in the cytoplasm may be lost in small germ cells.

The regulation of physiological germ cell death by cell size probably serves to maintain germline homeostasis and ensure the reallocation of resources from the dying to the surviving germ cells that grow in size while initiating oogenesis [13,15]. The coupling of nutrient signals sensed by the DAF-2 insulin receptor to the RAS/MAPK pathway could be a mechanism that permits the animals to adapt the equilibrium between oocyte differentiation and germ cell death to changing environmental conditions [29].

Cell shrinkage is a hallmark of cells undergoing apoptosis [36]. In most cases, the size reduction has been seen as a consequence rather than a cause of apoptotic cell death. Our findings that actomyosin-induced cell constriction is one factor in selecting smaller germ cells to undergo apoptosis could point to a more widely used mechanism. Even though the *C. elegans* hermaphrodite gonads with their syncytial architecture in the distal region represent a special case, it is conceivable that actomyosin-mediated cell shape changes, for example during asymmetric cell division, could contribute to the elimination of the usually smaller daughter cells [61,63].

Figure 7

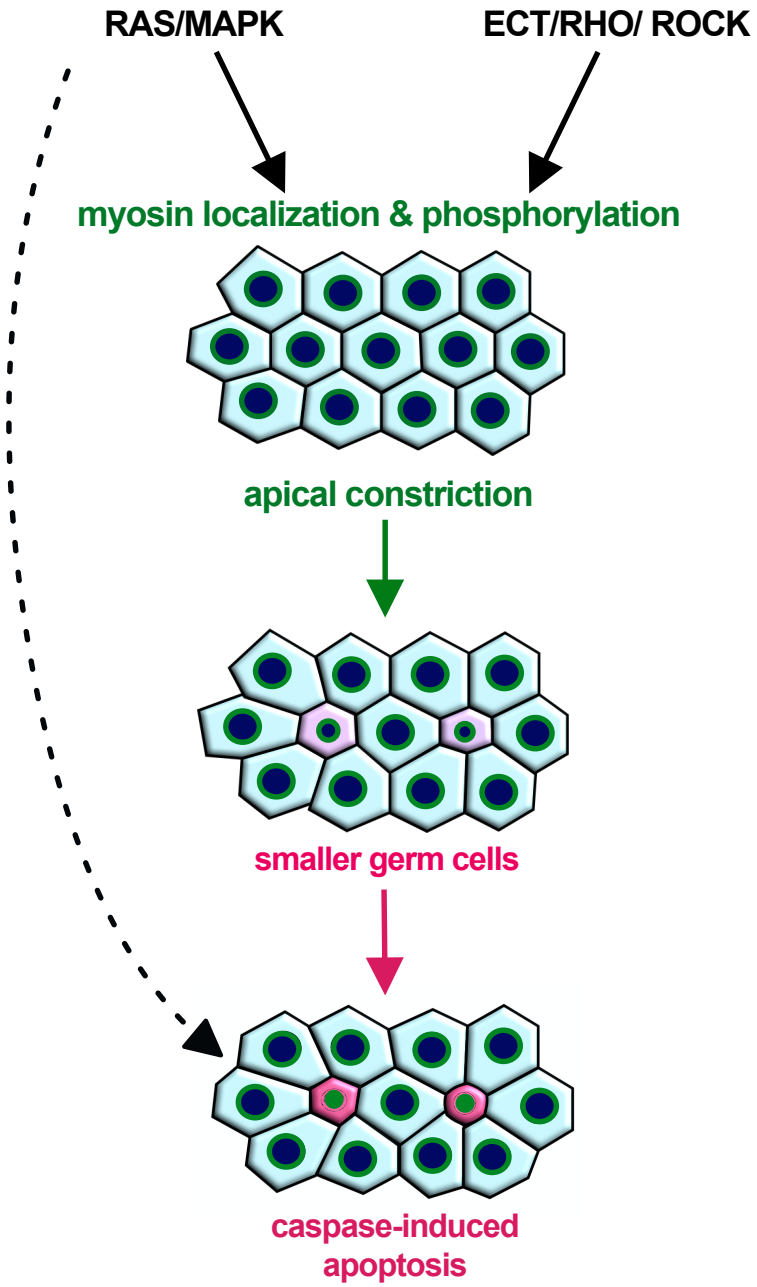

Figure. 7 Apical germ cell constriction promotes physiological germ cell death

Activation of RAS/MAPK signaling in germ cells at the pachytene stage is necessary for the localization of NMY-2 myosin at the rachis bridges, while ECT-2/RHO/ROCK signaling regulates actomyosin-contractility via phosphorylation of the regulatory myosin light chain MLC-4. Actomyosin contractility at the rachis bridges controls germ cell size and enhances stochastic disparities in germ cell sizes (Laplace effect). Smaller germ cells are selectively eliminated by Caspase-induced apoptosis. In addition, RAS/MAPK signaling may also directly induce apoptosis through unknown mechanisms (dashed arrow). Rachis bridges are

symbolized with green circles, cells that decrease in size are shown in pink and round, and apoptotic cells in magenta color.

Materials and Methods

C. elegans culture and maintenance

C. elegans strains were maintained at 20°C, unless noted otherwise, on standard nematode growth medium (NGM) agar plates as described [64]. The wild-type N2 strain was *C. elegans*, variety Bristol. We refer to translational protein fusions with a :: symbol between the gene and the tag used, and to transcriptional fusion with a > between the enhancer/promoter used and the gene of interest. Details on the construction of the plasmid vectors can be found in **suppl. Tab. S2**. The genotypes of the strains, the plasmid vectors, oligonucleotides, and sgRNAs used in this study are listed in **suppl. Tab. S3**.

Generation of alleles by CRISPR/CAS9 genome editing

The endogenous *ect-2(zh135)* and *let-502(zh139) gfp* insertions were generated using the modified CRISPR/CAS9 protocol described by [65]. The GFP tag was inserted at the C-terminus of *ect-2* and the N-terminus of *let-502*. The *mpk-1b(zh164)* allele introducing a stop codon at position 4 was generated by the co-CRISPR protocol described in [1].

Generation of extrachromosomal arrays by microinjection

Microinjection for the generation of the extrachromosomal line (*mpk-1(ga111^{ts}) unc-79(e1068)* III; *bcIs39[Plim-7::ced-1::gfp]; zhEx676[mpk-1A(+)]* V) was performed as described in [66] using purified PCR DNA at a concentration of 35 ng/µl and the co-injection marker pCFJ90 (P_{myo-2}>mCherry) at a concentration of 2.5 ng/µl [67]. pBluescript-KS was added to achieve the final DNA concentration of 150 ng/µl in a total volume of 20µl. Primary transformants were identified by the mCherry signal from the pharynx.

RNA interference

RNAi interference was done by feeding dsRNA-producing *E. coli* [68]. dsRNA-producing bacterial clones targeting genes of interest were obtained from the *C. elegans* genome-wide RNAi library or the *C. elegans* open reading frame (ORFeome) RNAi library (both from Source BioScience). Bacteria were grown in 2mL of 2xTY medium, containing 200µg/mL ampicillin and 25µg/mL tetracycline at 37°C and either directly seeded on NGM plates containing 3mM IPTG or diluted into fresh 2xTY medium containing 200µg/mL ampicillin and 25µg/mL tetracycline and 1mM IPTG and grown for 4 hours at 37°C before seeding [69]. For constitutive RNAi, larvae were synchronized at the L1 stage by hypochlorite treatment of

742 gravid adults and plated on NGM plates containing dsRNA-expressing bacteria. P0 animals
743 were analyzed after 72 to 74 hours of treatment (one-day-old adults). For transient RNAi,
744 synchronized L1 larvae were grown for 48 hours on OP50 bacteria and transferred as L4 larvae
745 to the RNAi plates for 24 hours.
746
747 **Microscopy**
748 Fluorescent and DIC (Nomarski) images were acquired on an Olympus BX61 microscope
749 equipped with an X-light V2 spinning disk confocal system (50µm pinhole diameter),
750 Prizmatix UHP-T-460-DI/UHP-T-560-DI LEDs as light source, an Andor iXon Ultra 888
751 EMCCD camera and a 60x or 100x Plan Apo lens (N.A. 1.3 and 1.4, respectively) or on a Leica
752 DMRA microscope equipped with a Lumencor Spectra light engine, two Hamamatsu C11400-
753 42U30 camera, a beam splitter and a 63x Plan Apo lens (N.A. 1.3). Long-term time-lapse
754 recordings were acquired on a Nikon Ti-U microscope equipped with an Omicron LedHUB as
755 a light source, a Photometrics Prime 95B camera and a PLAN Apo Lambda 60x oil immersion
756 objective. z-stacks were recorded with a spacing of 0.1 to 0.5 µm depending on the
757 magnification used. For germ-cell tracking experiments, one-day-old adult hermaphrodites
758 were immobilized in custom-made microfluidic devices as described [12], and 41 z-slices were
759 recorded every 7.5 minutes over 12 hours. See the **extended methods** section for a detailed
760 description of the image processing workflow.
761
762 **Scoring the apoptotic cell numbers**
763 Cell corpses were counted using strains containing the *bcIs39[Plim-7::ced-1::gfp]* reporter by
764 observing CED-1::GFP expression to identify corpses engulfed by the somatic sheath cells
765 [14,37]. Corpses were counted in one-day-old adults 72h after L1 synchronization at 20°C or,
766 where indicated, worms were incubated for 68h at 20°C and shifted to 25°C for 4 hours or 24
767 hours before quantification.
768
769 **Quantification of ERK phosphorylation by Western Blot analysis**
770 One-hundred one-day-old adult animals, grown from the L1 stage for 72 hours at 20°C or
771 incubated for the last 4 or 24 hours at 25°C where indicated, were washed 3 times in ice-cold
772 M9, collected by centrifugation and lysed in 50 µl 1xSDS samples buffer for 5 minutes at 95°C.
773 To remove genomic DNA, 1µl of RNase-Free DNase (QIAGEN) was added and the samples
774 were incubated at room temperature for 10 minutes, and again for 5 minutes at 95°C

775 immediately before loading. 20 µl extract each were loaded on two 4-12% gradient
776 polyacrylamide gels (Invitrogen) run in parallel. Western blots were incubated with anti-di-
777 phospho or total MAP Kinase antibodies as well as anti-alpha Tubulin antibodies as loading
778 controls. Bound primary antibodies were detected with HRP-conjugated secondary antibodies
779 followed by a chemiluminescence assay (SuperSignal™ West Dura Extended Duration
780 Substrate, Thermo Scientific). To inactivate HRP-conjugates and proceed with the incubation
781 of the primary anti-alpha tubulin antibody, the Western blots were incubated in sodium azide
782 for 1 hour. Bound primary antibodies were detected with HRP-conjugated secondary antibody
783 and chemiluminescence assay (SuperSignal™ West Pico PLUS Chemiluminescent Substrate,
784 Thermo Scientific). Total and di-phospho MPK-1B and alpha-tubulin levels were quantified
785 by measuring the corresponding band intensities using built-in measurement tools of Fiji [70].
786 Di-phosphorylated MPK-1B and total MPK-1B intensities were normalized to the alpha-
787 tubulin signals as loading controls before the di-phospho to total MPK-1B ratios were
788 calculated. The ratios shown in the graph **Fig. 6C'** are the average values of three biological
789 replicates (two for *let-502(lf)*), normalized in each experiment to the rations measured for the
790 wild-type controls. Antibodies used: anti-diphosphoERK, activated (Sigma-Aldrich, M8159);
791 anti-MAP Kinase (Sigma-Aldrich, M5670), anti-alpha tubulin (Abcam, ab18251), anti-alpha
792 Tubulin (Sigma-Aldrich, T6074), HRP anti-Rabbit (Jackson Immuno Research, 111-035-144)
793 and HRP anti-Mouse (Jackson Immuno Research, 115-035-146).
794
795 **Laser incision and recoil measurements**
796 Laser incisions were generated using an Olympus IXplore SpinSR10 microscope equipped
797 with a 355 nm pulsed laser for photomanipulation (UGA-42 Caliburn, Rapp Optoelectronics),
798 a z-drift compensator (IX3-ZDC2, Olympus) and a Hamamatsu ORCA-Fusion sCMOS
799 camera, using a 60x Plan UPlan Apo Silicone oil immersion lens (N.A. 1.3). Incisions were
800 made with 1000 msec laser pulses at 8-10% laser power. Animals mounted on agarose pads
801 were observed for 2 frames before and 60 frames after the incision at a rate of 1.33 frames per
802 sec. For quantification, three to four bright NMY-2::GFP foci around the incision point were
803 manually tracked over 40 frames using Fiji software [70] to measure their relative displacement
804 from the point of incision, from which the average radial displacement (recoil) for each animal
805 and time point was calculated (**suppl. Tab. S1**). Curve-fitting was done individually for each
806 animal recorded using the equation:
807 $$recoil(t) = initial\ recoil\ velocity/k * (1-e^{-k*t})$$

to estimate the initial recoil velocity (= ∂recoil(0)/∂t) and the total recoil (recoil(∞) = initial recoil velocity/k, where k = Elasticity of the tissue/viscosity coefficient of the drag in the cytoplasm) using Graph Pad Prism software as described [53]. Since we quantified the radial displacement rather than the change in diameter of the opening, the values obtained are approximately half of those reported by [18].

Statistical analysis

GraphPad Prism 9.0 was used to perform statistical tests and results are shown in **suppl. Tab. S1**. We used two-tailed unpaired t-tests when comparing two samples or ANOVA with Tukey's correction for multiple comparisons when comparing more than two samples to calculate the p-values. Samples sizes (numbers of animals or cells analyzed) are indicated in the figure legends for each experiment. All the experiments were repeated with at least 3 independent biological replicates, except for **Fig. 3I** (left), **Fig. 4A** and **Fig.4B** (*mpk-1b(zh164)*) with 2 biological replicates).

Author contributions

Conceptualization: T.K. and A.H.; Investigation: T.K., S.B., A.C.L. and A.H.; Formal Analysis: T.K., S.B. and T.A.; Writing - Original Draft: T.K. and A.H.; Writing - Review & Editing: T.K., S.B., T.A., A.C.L., A.dM. and A.H.; Funding acquisition: T.K., A.dM. and A.H.

Acknowledgments

We thank all present and past members of the Hajnal group for critical discussion and comments, Michael Daube for lab assistance, and Michael Walser for help with the illustrations. We thank Anne-Lise Routier-Kierzkowska and Richard Smith for their help with using MorphographX software. We are also grateful to Barbara Conradt for sharing the MD4476 strain and helpful comments and Andrew Fire for vectors and J. Ahringer for RNAi clones and WormBase. We thank the team of the Center for Microscopy and Image Analysis, University of Zurich, for their assistance with performing the laser cutting experiments. Some strains were provided by the CGC, which is funded by the NIH Office of Research Infrastructure Programs (P40 OD010440). This project was supported by the Kanton Zürich, the ETH Zürich, grant no. FK-20-090 from the Forschungskredit of the University of Zürich to T.K. and by the Swiss National Science Foundation grant no. 31003A- 166580 to A.H.

Competing interests

The authors declare that no competing interests exist.

References

1. Arya R, White K. Cell death in development: signaling pathways and core mechanisms. Semin Cell Dev Biol. 2015;39: 12–19. doi:10.1016/j.semcdb.2015.02.001

2. Vaux DL, Korsmeyer SJ. Cell Death in Development. Cell. 1999;96: 245–254. doi:10.1016/S0092-8674(00)80564-4

3. Jacobson MD, Weil M, Raff MC. Programmed cell death in animal development. Cell. 1997;88: 347–354. doi:10.1016/s0092-8674(00)81873-5

4. Fuchs Y, Steller H. Programmed cell death in animal development and disease. Cell. 2011;147: 742–758. doi:10.1016/j.cell.2011.10.033

5. Horvitz HR. Genetic control of programmed cell death in the nematode Caenorhabditis elegans. Cancer Res. 1999;59: 1701s–1706s.

6. Sulston JE, Horvitz HR. Post-embryonic cell lineages of the nematode, Caenorhabditis elegans. Dev Biol. 1977;56: 110–156.

7. Lettre G, Hengartner MO. Developmental apoptosis in C. elegans: a complex CEDnario. Nat Rev Mol Cell Biol. 2006;7: 97–108. doi:10.1038/nrm1836

8. Conradt B, Wu Y-C, Xue D. Programmed Cell Death During Caenorhabditis elegans Development. Genetics. 2016;203: 1533–1562. doi:10.1534/genetics.115.186247

9. Conradt B, Xue D. Programmed cell death. WormBook Online Rev C Elegans Biol. 2005; 1–13. doi:10.1895/wormbook.1.32.1

10. Sulston JE, Schierenberg E, White JG, Thomson JN. The embryonic cell lineage of the nematode Caenorhabditis elegans. Dev Biol. 1983;100: 64–119.

11. Gumienny TL, Lambie E, Hartwieg E, Horvitz HR, Hengartner MO. Genetic control of programmed cell death in the Caenorhabditis elegans hermaphrodite germline. Dev Camb Engl. 1999;126: 1011–1022.

12. Berger S, Lattmann E, Aegerter-Wilmsen T, Hengartner M, Hajnal A, deMello A, et al. Long-term C. elegans immobilization enables high-resolution developmental studies in vivo. Lab Chip. 2018;18: 1359–1368. doi:10.1039/c7lc01185g

13. Gartner A, Boag PR, Blackwell TK. Germline survival and apoptosis. WormBook Online Rev C Elegans Biol. 2008; 1–20.

14. Zhou Z, Hartwieg E, Horvitz HR. CED-1 Is a Transmembrane Receptor that Mediates Cell Corpse Engulfment in C. elegans. Cell. 2001;104: 43–56. doi:10.1016/S0092-8674(01)00190-8

15. Wolke U, Jezuit EA, Priess JR. Actin-dependent cytoplasmic streaming in C. elegans oogenesis. Dev Camb Engl. 2007;134: 2227–2236. doi:10.1242/dev.004952

16. Hirsh D, Oppenheim D, Klass M. Development of the reproductive system of Caenorhabditis elegans. Dev Biol. 1976;49: 200–219. doi:10.1016/0012-1606(76)90267-0

17. Kimble J. Germline proliferation and its control. WormBook Online Rev C Elegans Biol. 2005; 1–14. doi:10.1895/wormbook.1.13.1

18. Priti A, Ong HT, Toyama Y, Padmanabhan A, Dasgupta S, Krajnc M, et al. Syncytial germline architecture is actively maintained by contraction of an internal actomyosin corset. Nat Commun. 2018;9: 4694. doi:10.1038/s41467-018-07149-2

884 19. Rehain-Bell K, Love A, Werner ME, MacLeod I, Yates JR, Maddox AS. A Sterile 20-
885 family kinase and its co-factor CCM-3 regulate contractile ring proteins on germline
886 intercellular bridges. Curr Biol CB. 2017;27: 860–867. doi:10.1016/j.cub.2017.01.058

887 20. Burridge K, Wennerberg K. Rho and Rac Take Center Stage. Cell. 2004;116: 167–179.
888 doi:10.1016/S0092-8674(04)00003-0

889 21. Schwartz M. Rho signalling at a glance. J Cell Sci. 2004;117: 5457–5458.
890 doi:10.1242/jcs.01582

891 22. Saadeldin IM, Tukur HA, Aljumaah RS, Sindi RA. Rocking the Boat: The Decisive Roles
892 of Rho Kinases During Oocyte, Blastocyst, and Stem Cell Development. Front Cell Dev Biol.
893 2021;8: 616762. doi:10.3389/fcell.2020.616762

894 23. Canevascini S, Marti M, Fröhli E, Hajnal A. The Caenorhabditis elegans homologue of
895 the proto-oncogene ect-2 positively regulates RAS signalling during vulval development.
896 EMBO Rep. 2005;6: 1169–1175. doi:10.1038/sj.embor.7400574

897 24. Wissmann A, Ingles J, McGhee JD, Mains PE. Caenorhabditis elegans LET-502 is related
898 to Rho-binding kinases and human myotonic dystrophy kinase and interacts genetically with a
899 homolog of the regulatory subunit of smooth muscle myosin phosphatase to affect cell shape.
900 Genes Dev. 1997;11: 409–422. doi:10.1101/gad.11.4.409

901 25. Piekny AJ, Mains PE. Rho-binding kinase (LET-502) and myosin phosphatase (MEL-11)
902 regulate cytokinesis in the early Caenorhabditis elegans embryo. J Cell Sci. 2002;115: 2271–
903 2282.

904 26. Gally C, Wissler F, Zahreddine H, Quintin S, Landmann F, Labouesse M. Myosin II
905 regulation during C. elegans embryonic elongation: LET-502/ROCK, MRCK-1 and PAK-1,
906 three kinases with different roles. 2009;136: 3109–3119. doi:10.1242/dev.039412

907 27. Martin E, Harel S, Nkengfac B, Hamiche K, Neault M, Jenna S. pix-1 Controls Early
908 Elongation in Parallel with mel-11 and let-502 in Caenorhabditis elegans. PLoS ONE. 2014;9:
909 e94684. doi:10.1371/journal.pone.0094684

910 28. Drewnik ED, Wiesenfahrt T, Smit RB, Park Y-J, Pallotto LM, Mains PE. Tissue-specific
911 regulation of epidermal contraction during Caenorhabditis elegans embryonic morphogenesis.
912 G3 GenesGenomesGenetics. 2021;11: jkab164. doi:10.1093/g3journal/jkab164

913 29. Lopez AL, Chen J, Joo H-J, Drake M, Shidate M, Kseib C, et al. DAF-2 and ERK couple
914 nutrient availability to meiotic progression during Caenorhabditis elegans oogenesis. Dev Cell.
915 2013;27: 227–240.

916 30. Rutkowski R, Dickinson R, Stewart G, Craig A, Schimpl M, Keyse SM, et al. Regulation
917 of Caenorhabditis elegans p53/CEP-1-dependent germ cell apoptosis by Ras/MAPK signaling.
918 Engebrecht J, editor. PLoS Genet. 2011;7: e1002238. doi:10.1371/journal.pgen.1002238

919 31. Chartier NT, Mukherjee A, Pfanzelter J, Fürthauer S, Larson BT, Fritsch AW, et al. A
920 hydraulic instability drives the cell death decision in the nematode germline. Nat Phys.
921 2021;17: 920–925. doi:10.1038/s41567-021-01235-x

922 32. Raiders SA, Eastwood MD, Bacher M, Priess JR. Binucleate germ cells in Caenorhabditis
923 elegans are removed by physiological apoptosis. PLoS Genet. 2018;14: e1007417.
924 doi:10.1371/journal.pgen.1007417

925 33. Barbier de Reuille P, Routier-Kierzkowska A-L, Kierzkowski D, Bassel GW, Schüpbach
926 T, Tauriello G, et al. MorphoGraphX: A platform for quantifying morphogenesis in 4D. eLife.
927 2015;4: 05864. doi:10.7554/eLife.05864

928 34. Dickinson DJ, Ward JD, Reiner DJ, Goldstein B. Engineering the Caenorhabditis elegans
929 genome using Cas9-triggered homologous recombination. Nat Methods. 2013;10: 1028–1034.
930 doi:10.1038/nmeth.2641

931 35. Ellis HM, Horvitz HR. Genetic control of programmed cell death in the nematode C.
932 elegans. Cell. 1986;44: 817–829. doi:10.1016/0092-8674(86)90004-8

933 36. Kerr JFR, Wyllie AH, Currie AR. Apoptosis: A Basic Biological Phenomenon with Wide-
934 ranging Implications in Tissue Kinetics. Br J Cancer. 1972;26: 239–257.

935 37. Lu N, Yu X, He X, Zhou Z. Detecting Apoptotic Cells and Monitoring Their Clearance in
936 the Nematode Caenorhabditis elegans. Methods Mol Biol Clifton NJ. 2009;559: 357–370.
937 doi:10.1007/978-1-60327-017-5_25

938 38. Yu X, Lu N, Zhou Z. Phagocytic Receptor CED-1 Initiates a Signaling Pathway for
939 Degrading Engulfed Apoptotic Cells. PLoS Biol. 2008;6: e61.
940 doi:10.1371/journal.pbio.0060061

941 39. Derry WB, Putzke AP, Rothman JH. Caenorhabditis elegans p53: Role in Apoptosis,
942 Meiosis, and Stress Resistance. Science. 2001;294: 591–595. doi:10.1126/science.1065486

943 40. Nadarajan S, Mohideen F, Tzur YB, Ferrandiz N, Crawley O, Montoya A, et al. The MAP
944 kinase pathway coordinates crossover designation with disassembly of synaptonemal complex
945 proteins during meiosis. eLife. 2016;5: e12039. doi:10.7554/eLife.12039

946 41. Bhalla N, Dernburg AF. A conserved checkpoint monitors meiotic chromosome synapsis
947 in Caenorhabditis elegans. Sci N Y NY. 2005;310: 1683–1686. doi:10.1126/science.1117468

948 42. Zou L, Wu D, Zang X, Wang Z, Wu Z, Chen D. Construction of a germline-specific RNAi
949 tool in C. elegans. Sci Rep. 2019;9: 2354. doi:10.1038/s41598-019-38950-8

950 43. Liu J, Maduzia LL, Shirayama M, Mello CC. NMY-2 maintains cellular asymmetry and
951 cell boundaries, and promotes a SRC-dependent asymmetric cell division. Dev Biol. 2010;339:
952 366–373. doi:10.1016/j.ydbio.2009.12.041

953 44. Kritikou EA, Milstein S, Vidalain P-O, Lettre G, Bogan E, Doukoumetzidis K, et al. C.
954 elegans GLA-3 is a novel component of the MAP kinase MPK-1 signaling pathway required
955 for germ cell survival. Genes Dev. 2006;20: 2279–2292. doi:10.1101/gad.384506

956 45. Lee M-H, Hook B, Pan G, Kershner AM, Merritt C, Seydoux G, et al. Conserved
957 regulation of MAP kinase expression by PUF RNA-binding proteins. PLoS Genet. 2007;3:
958 e233. doi:10.1371/journal.pgen.0030233

959 46. Church DL, Guan KL, Lambie EJ. Three genes of the MAP kinase cascade, mek-2, mpk-
960 1/sur-1 and let-60 ras, are required for meiotic cell cycle progression in Caenorhabditis elegans.
961 1995;121: 2525–2535.

962 47. Lee M-H, Ohmachi M, Arur S, Nayak S, Francis R, Church D, et al. Multiple functions
963 and dynamic activation of MPK-1 extracellular signal-regulated kinase signaling in
964 Caenorhabditis elegans germline development. Genetics. 2007;177: 2039–2062.

965 48. Das D, Chen S-Y, Arur S. ERK phosphorylates chromosomal axis component HORMA
966 domain protein HTP-1 to regulate oocyte numbers. Sci Adv. 2020;6: eabc5580.
967 doi:10.1126/sciadv.abc5580

968 49. Lackner MR, Kim SK. Genetic analysis of the Caenorhabditis elegans MAP kinase gene
969 mpk-1. Genetics. 1998;150: 103–117.

970 50. Eisenmann DM, Kim SK. Mechanism of activation of the Caenorhabditis elegans ras
971 homologue let-60 by a novel, temperature-sensitive, gain-of-function mutation. Genetics.
972 1997;146: 553–565.

973 51. Yang Q, Roiz D, Mereu L, Daube M, Hajnal A. The Invading Anchor Cell Induces Lateral
974 Membrane Constriction during Vulval Lumen Morphogenesis in C. elegans. Dev Cell.
975 2017;42: 271-285.e3. doi:10.1016/j.devcel.2017.07.008

976 52. Stringer C, Wang T, Michaelos M, Pachitariu M. Cellpose: a generalist algorithm for
977 cellular segmentation. Nat Methods. 2021;18: 100–106. doi:10.1038/s41592-020-01018-x

978 53. Liang X, Michael M, Gomez G. Measurement of Mechanical Tension at cell-cell junctions
979 using two-photon laser ablation. BIO-Protoc. 2016;6. doi:10.21769/BioProtoc.2068

980 54. Verlhac M-H, de Pennart H, Maro B, Cobb MH, Clarke HJ. MAP Kinase Becomes Stably
981 Activated at Metaphase and Is Associated with Microtubule-Organizing Centers during
982 Meiotic Maturation of Mouse Oocytes. Dev Biol. 1993;158: 330–340.
983 doi:10.1006/dbio.1993.1192

984 55. Ivanovska I, Lee E, Kwan KM, Fenger DD, Orr-Weaver TL. The Drosophila MOS
985 Ortholog Is Not Essential for Meiosis. Curr Biol. 2004;14: 75–80.
986 doi:10.1016/j.cub.2003.12.031

987 56. Fan H-Y, Sun Q-Y. Involvement of mitogen-activated protein kinase cascade during
988 oocyte maturation and fertilization in mammals. Biol Reprod. 2004;70: 535–547.
989 doi:10.1095/biolreprod.103.022830

990 57. Miller MA, Nguyen VQ, Lee M-H, Kosinski M, Schedl T, Caprioli RM, et al. A Sperm
991 Cytoskeletal Protein That Signals Oocyte Meiotic Maturation and Ovulation. Science.
992 2001;291: 2144–2147. doi:10.1126/science.1057586

993 58. Arur S, Ohmachi M, Berkseth M, Nayak S, Hansen D, Zarkower D, et al. MPK-1 ERK
994 controls membrane organization in C. elegans oogenesis via a sex determination module. Dev
995 Cell. 2011;20: 677–688. doi:10.1016/j.devcel.2011.04.009

996 59. Vicente-Manzanares M, Ma X, Adelstein RS, Horwitz AR. Cytoskeletal motors: Non-
997 muscle myosin II takes centre stage in cell adhesion and migration. 2009; 1–13.
998 doi:10.1038/nrm2786

999 60. Offenburger S-L, Bensaddek D, Murillo AB, Lamond AI, Gartner A. Comparative genetic,
1000 proteomic and phosphoproteomic analysis of C. elegans embryos with a focus on ham-1/STOX
1001 and pig-1/MELK in dopaminergic neuron development. Sci Rep. 2017;7: 4314.
1002 doi:10.1038/s41598-017-04375-4

1003 61. Wei H, Lambie EJ, Osório DS, Carvalho AX, Conradt B. PIG-1 MELK-dependent
1004 phosphorylation of nonmuscle myosin II promotes apoptosis through CES-1 Snail partitioning.
1005 PLoS Genet. 2020;16: e1008912. doi:10.1371/journal.pgen.1008912

1006 62. Pourkarimi E, Greiss S, Gartner A. Evidence that CED-9/Bcl2 and CED-4/Apaf-1
1007 localization is not consistent with the current model for C. elegans apoptosis induction. Cell
1008 Death Differ. 2011;19: 406–415. doi:10.1038/cdd.2011.104

1009 63. Ou G, Stuurman N, D'Ambrosio M, Vale RD. Polarized Myosin Produces Unequal-Size
1010 Daughters During Asymmetric Cell Division. Science. 2010;330: 677–680.
1011 doi:10.1126/science.1196112

1012 64. Brenner S. The genetics of Caenorhabditis elegans. Genetics. 1974;77: 71–94.

1013 65. Dickinson DJ, Goldstein B. CRISPR-Based Methods for Caenorhabditis elegans Genome
1014 Engineering. Genetics. 2016;202: 885–901. doi:10.1534/genetics.115.182162

1015 66. Mello CC, Kramer JM, Stinchcomb D, Ambros V. Efficient gene transfer in C.elegans:
1016 extrachromosomal maintenance and integration of transforming sequences. EMBO J. 1991;10:
1017 3959–3970.

1018 67. Frøkjær-Jensen C, Davis MW, Ailion M, Jorgensen EM. Improved Mos1-mediated
1019 transgenesis in C. elegans. Nat Methods. 2012;9: 117–118. doi:10.1038/nmeth.1865

1020 68. Kamath R. Genome-wide RNAi screening in Caenorhabditis elegans. Methods. 2003;30:
1021 313–321. doi:10.1016/S1046-2023(03)00050-1

1022 69. Xiao R, Chun L, Ronan EA, Friedman DI, Liu J, Xu XZS. RNAi Interrogation of Dietary
1023 Modulation of Development, Metabolism, Behavior, and Aging in C. elegans. Cell Rep.
1024 2015;11: 1123–1133. doi:10.1016/j.celrep.2015.04.024

1025 70. Schindelin J, Arganda-Carreras I, Frise E, Kaynig V, Longair M, Pietzsch T, et al. Fiji: an
1026 open-source platform for biological-image analysis. Nat Methods. 2012;9: 676–682.
1027 doi:10.1038/nmeth.2019

1028

Supplementary information

Table of contents:

Supplementary figures

Figure S1

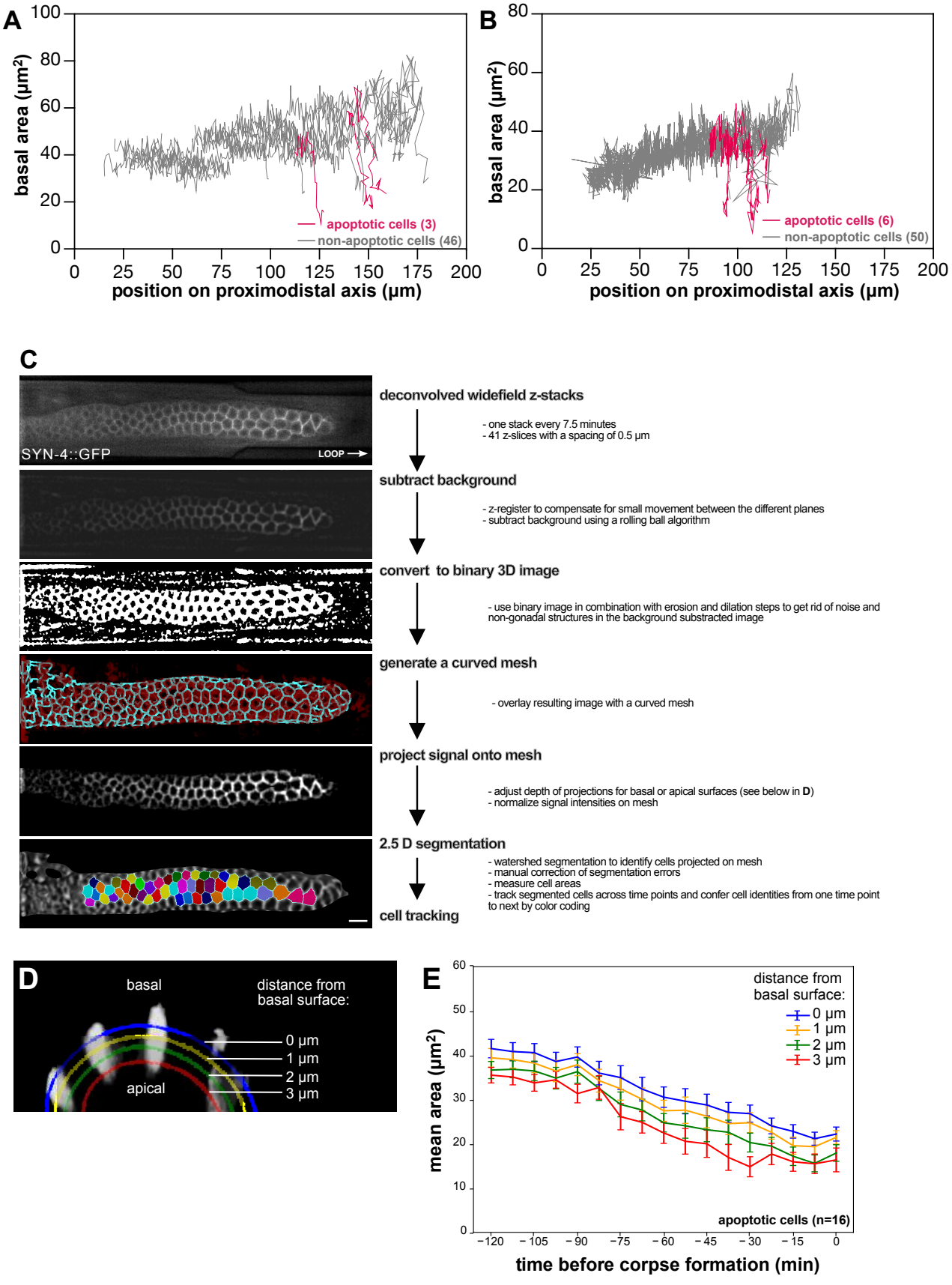

Suppl. Fig. S1 related to Fig. 1

(**A, B**) Results of cell tracking experiments in two additional wild-type animals as described in **Fig. 1F**. (**C**) MorphographX workflow to track germ cells as described in the **extended methods section**. Scale bar is 10 µm. (**D**) Projections of increasing depths were generated to measure the basal, middle and apical areas in MorphographX. (**E**) Plot showing the decrease in mean area ±SEM of apoptotic cell size before corpse formation in projections of increasing depths.

Figure S2

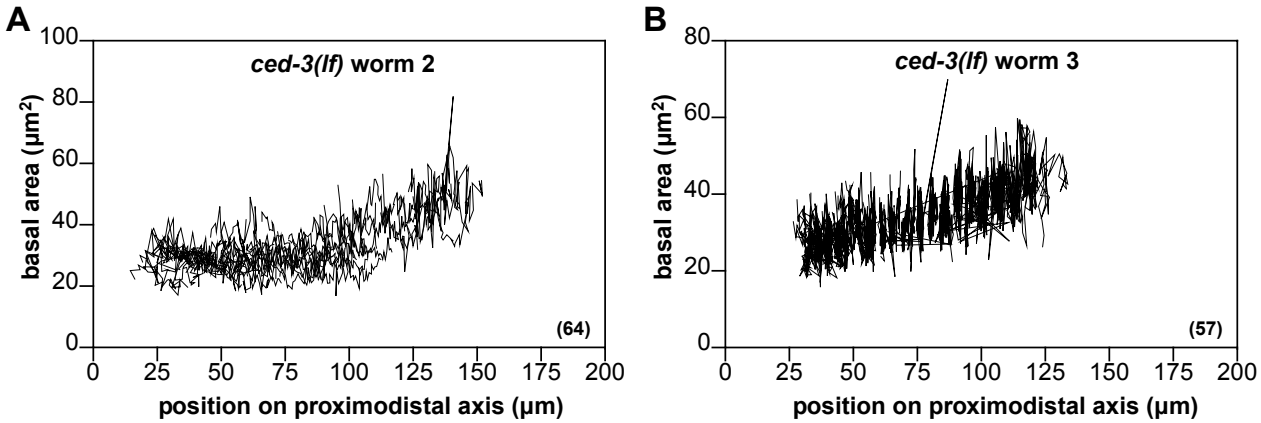

Suppl. Fig. S2 related to Fig. 2

(**A, B**) Results of germ cell tracking experiments in two additional *ced-3(lf)* animals, as described in **Fig. 2A**.

Figure S3

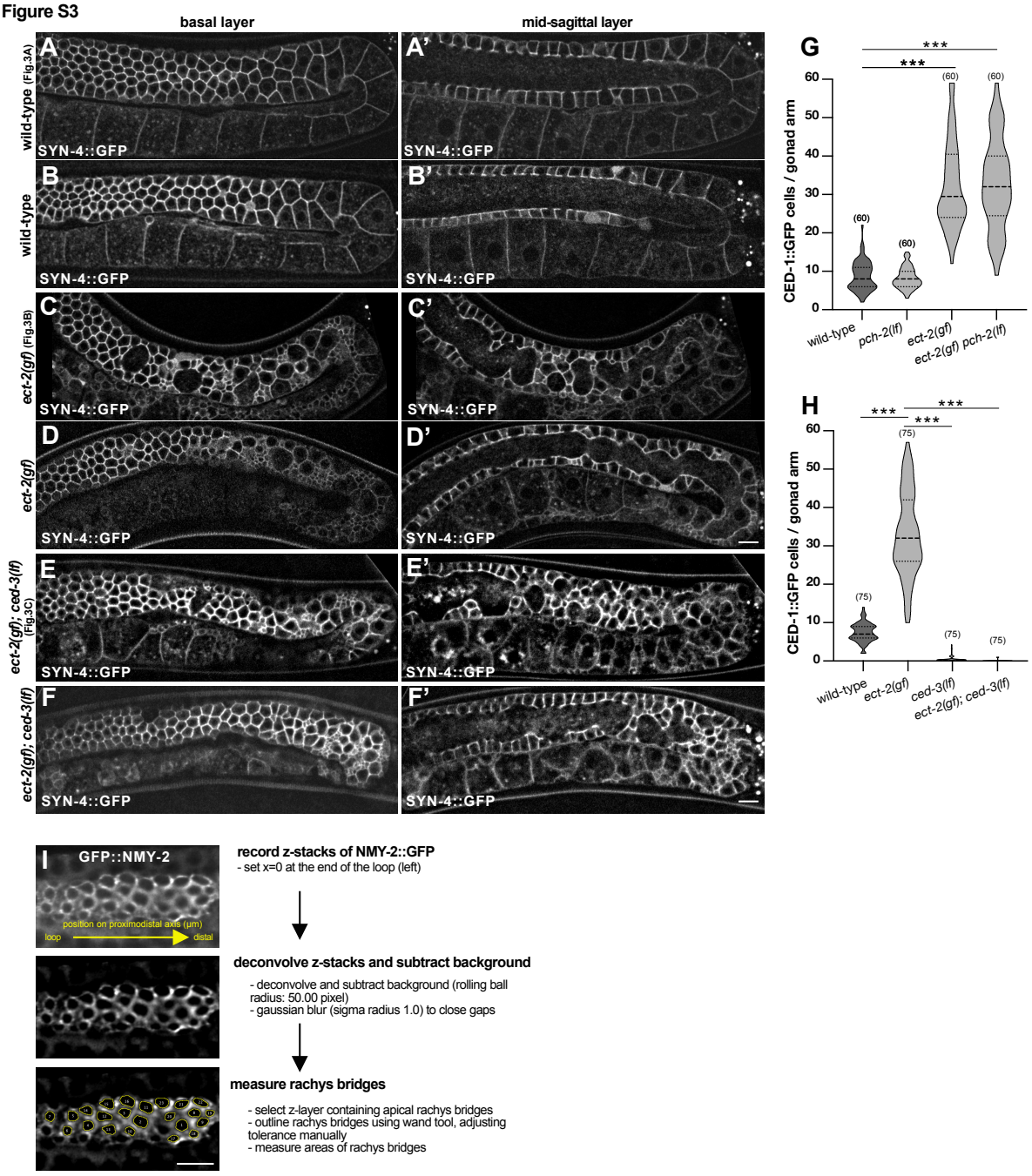

Suppl Fig. S3 related to Fig. 3

(**A-F'**) Full views of the SYN-4::GFP membrane marker in the gonad arms of the animals that are shown in **Fig. 3A-C**. For each genotype, one additional example is shown. Panels **A-F** show basal and panels **A'-F'** mid-sagittal sections. The scale bar is 10 µm. (**G, H**) Violin plots showing the number of CED-1::GFP positive apoptotic cells per gonad arm in one-day-old adults of the indicated genotypes. (**I**) Workflow used to measure the rachis bridge area in **Fig. 3G, Fig.5C, F & S5E**, as described in the **extended methods section**. Statistical analysis was done as described in the legend to **Fig. 3** and **suppl. Tab. S1**. The scale bar is 10 µm.

Figure S4

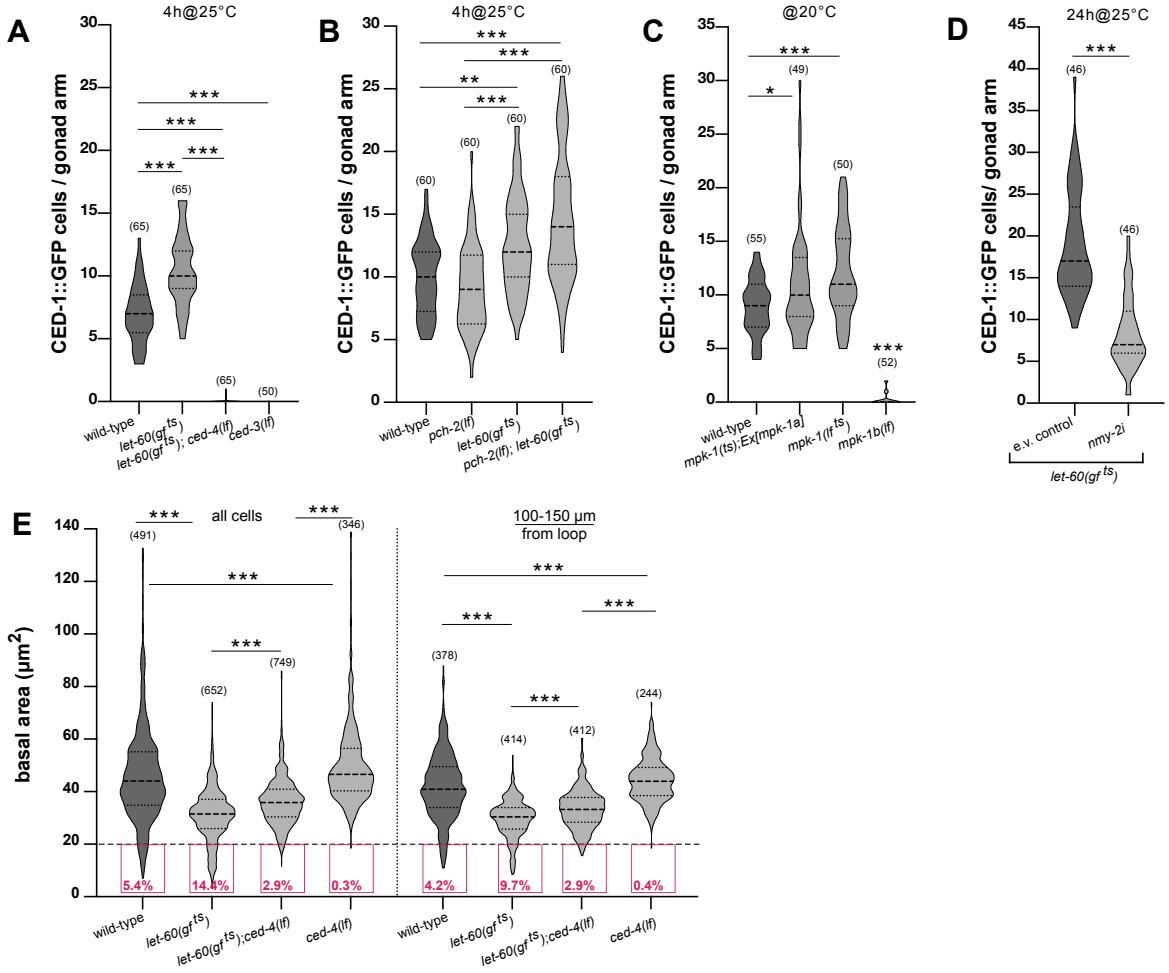

Suppl. Fig. S4 related to Fig.4

(**A**) Violin plot showing the number of CED-1::GFP positive apoptotic germ cells per gonad arm in one-day-old adults of the indicated genotypes after a 4-hour up-shift to the restrictive temperature (4h@25°C). (**B**) Violin plot showing the number of CED-1::GFP positive apoptotic germ cells of the indicated genotypes grown at 20°C for 68 hours and incubated for 4 hours at the restrictive temperature of 25°C. (**C**) Violin plot showing the number of CED-1::GFP positive apoptotic germ cells per gonad arm in one-day-old adults of the indicated genotypes continuously grown at 20°C (baseline control for **Fig. 4B**, right). (**D**) Violin plot showing the number of CED-1::GFP positive apoptotic germ cells per gonad arm in one-day-old adults after *nmy-2* RNAi treatment in the *let-60(gf^{ts})* background from the L4 stage with a simultaneous 24-hour up-shift to 25°C (24h@25°C). (**E**) Violin plot for the basal cell areas in the 0 – 150 µm and 100 – 150 µm regions, besides the 50-100 µm region shown in **Fig. 4D**. Statistical analysis was done as described in the legend to **Fig. 4** and **suppl. Tab. S1**. Scale bars are 10 µm.

Figure S5

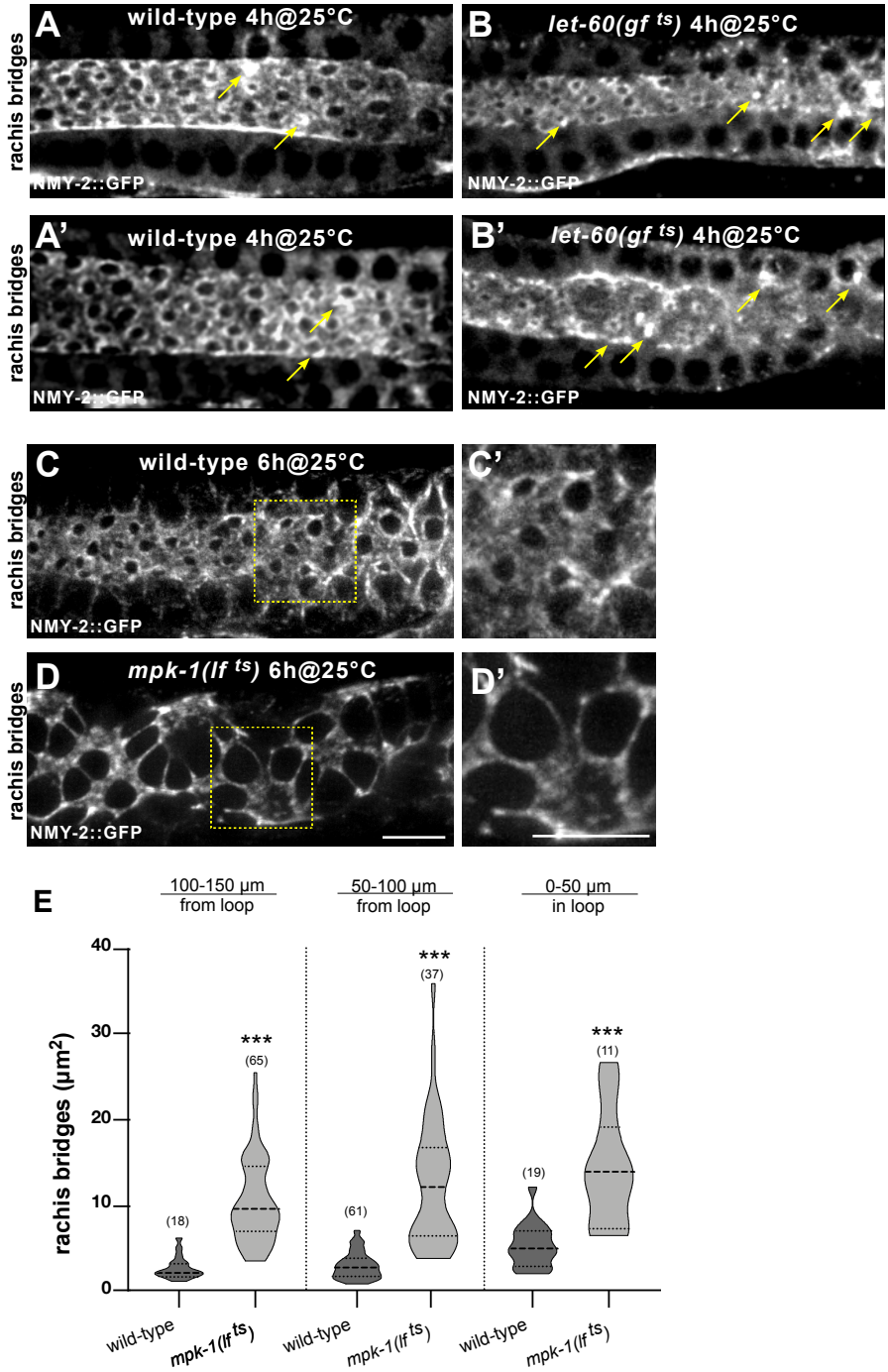

Supp. Fig. S5 related to Fig. 5

(**A-B'**) Additional examples of the rachis bridges outlined by NMY-2::GFP in wild-type and *let-60(gf^{ts})* animals. Note the yellow arrows pointing to fully enclosed rachis bridges appearing as bright NMY-2::GFP spots. (**C-D**) Rachis bridges outlined by NMY-2::GFP in young wild-type and *mpk-1(lf^{ts})* adults after a 6-hour up-shift to the restrictive temperature of 25°C. The shorter, 4 hours inactivation is shown in **Fig. 5D-E**. (**E**) Violin plots showing the size of the rachis bridges in wild-type and *mpk-1(lf^{ts})* mutants in the three indicated gonad regions after a 6-hour incubation at 25°C. Three animals were analyzed for each genotype. Scale bars are 10 µm.

Figure S6

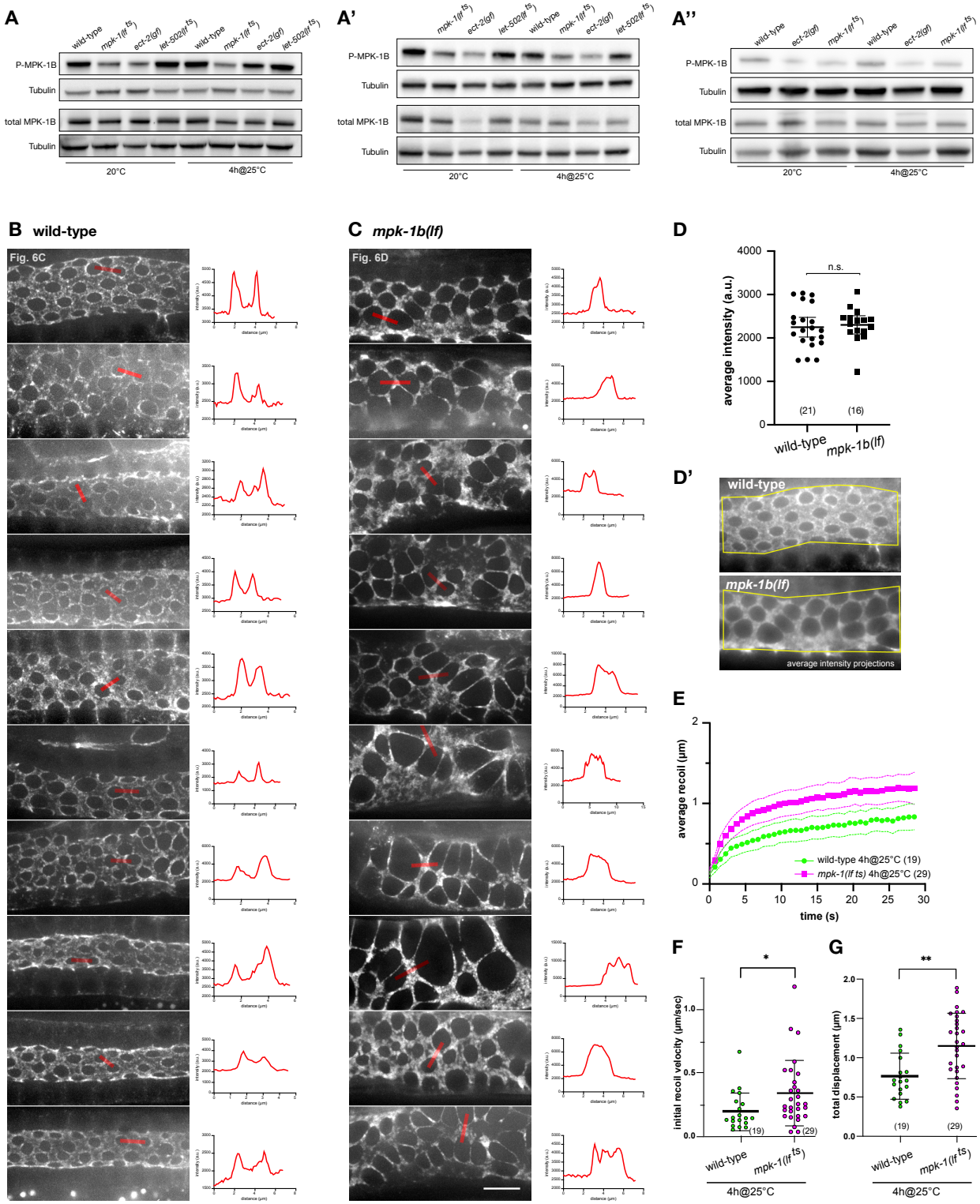

Supp. Fig. S6 related to Fig. 6

(**A**) Western blots used for the quantification of P-MPK-1B and total MPK-1B protein levels shown in **Fig. 6B**. One-day-old adults of the indicated genotypes were incubated either at 20°C for 72 hours after the L1 stage or for 4 hours at the restrictive temperature of 25°C before analysis. (**B**) Additional examples of NMY-2::GFP localization in the late pachytene region (50-100µm from the loop) of wild-type and (**C**) *mpk-1b(lf)* mutants one-day old adults (66-68

hours post-L1 arrest). Maximum intensity z-projections of flat field-corrected raw images (without deconvolution) are shown. The top panels are the same animals as in **Fig. 6C&D**. Relative intensity profiles along the regions indicated with red bars are shown to the right of each panel. Note the two peaks corresponding to the NMY-2::GFP signal at the rachis bridges in the wild-type, as opposed to the single peaks in *mpk-1b* mutants. (**D**) Quantification of NMY-2::GFP levels in wild-type and *mpk-1b(lf)* animals. Average intensity z-projections of flat field-corrected raw images were used for quantification of the mean NMY-2::GFP intensities on the apical cortex, as illustrated in (**D'**). (**E**) Mean radial displacement (recoil) plotted against time after incision, (**F**) Initial recoil velocities, and (**G**) total recoil in wild-type and *mpk-1(lf^{ts})* mutants grown for 4 hours at 25°C, calculated as described in the legend to **Fig. 6 F-H** and in materials and methods. See **suppl. Tab. S1** for the individual measurements of all animals scored. The horizontal bars indicate the mean values, the error bars the 95% CI and the numbers in brackets the numbers of animals analyzed. Scale bar in (**C**) is 10 µm.

Supplementary movies

Movie S1 Germ cell tracking of the wild-type animal shown in **Fig. 1B**.

Movie S2 Germ cell tracking of the *ced-3(lf)* mutant animal shown in **Fig. 2A**.

Movie S3 Recoil after laser incision in the wild-type animal shown in **Fig. 6E**.

Movie S4 Recoil after laser incision in the *mpk-1b(lf)* animal shown in **Fig. 6E'**.

Extended methods

Image processing

Images were processed using the Huygens Deconvolution platform (SVI, Center for Microscopy and Image Analysis, University of Zürich) or using the YacuDecu implementation of CUDA-based Richardson Lucy deconvolution in Matlab to remove background signals.

Germ cell size measurements and tracking

Generation of curved meshes and cell segmentation

Pre-processing of deconvolved image stacks of the SYN-4::GFP membrane marker at each time point was done using Fiji software [70], with z-registration to compensate for small movements of the worm in the microfluidic device and additional background subtraction (see attached Fiji scripts). Cells were tracked over time using a custom-made Python script attached below with the MorphoGraphX software package [33], which enables the analysis of cell shapes on curved surfaces as illustrated in **suppl. Figure S1C**. As a first step, regions of the distal gonad arms with pachytene stage germ cells were selected and processed using a combination of dilation and erosion (the highest or lowest value of a pixel and a defined neighborhood is taken, respectively). In short, the selection was based on the assumption that germline membranes form a somewhat regular polygonal pattern. When dilating this image with a bit more than half a cell diameter, the whole gonad fills up and the opposite erosion does not reverse the image to its original, but leaves the gonad filled. Other patterns were selected against, also using the fact that the position of the worm is always very similar when using the microfluidic devices. After gonad selection, a mesh was generated based on a threshold-like

mechanism that scans the image from the top to the bottom. After smoothening the mesh, its quality was checked visually and any artifacts were repaired by manual local smoothening. Such artifacts occurred in roughly 10% of the time points and were caused for example by signals that did not arise from germline cells or by small regions in the germline with relatively low signal intensity. The z-registered and background-subtracted 3D image was then projected onto the curved mesh enabling the analysis of the basal surface. Cells were segmented using a watershed algorithm for curved surfaces. The resulting segmentation of cells was checked and, if necessary, manually corrected. Areas at different distances from the basal surface (e.g. the apical surface) were obtained as follows. Using MorphoGraphX, a new mesh was created at 1, 2, or 3 µm absolute distance from the basal mesh on the apical side (**suppl. Figure S1D**). The signal of the registered and background-subtracted image was then projected onto this new mesh and cells were again segmented using a watershed algorithm.

Germ cell tracking on curved meshes

The gonad arms move considerably in the microfluidic device even when the animal is largely immobile, this is necessary to allow egg laying and to maintain normal gonad physiology [12]. Therefore, cell tracking was performed manually by manually overlaying meshes of two subsequent time points and conferring cell identities from one mesh to another. In this way, it was possible to compare the patterns globally and reliably identify cells across the time points.

Measuring cell sizes

Basal areas of the segmented cells were obtained using MorphoGraphX, which directly measures the mesh area occupied by each cell. Basal cell areas from single images were obtained using the same scripts but with different threshold values. The segmentation of the apoptotic cells was checked manually and improved if necessary. Some cells could not be analyzed at 3 µm (or rarely at 2 µm) distance from the basal surface at some time points due to variations in cell height. In these cases, the cells were excluded from the analysis at the corresponding depths and time points. Since the membrane signal decreases most apically, the number of manual improvements increased with increasing depth. Cell areas were obtained directly from the respective meshes.

Tracking of apical rachis bridges

To measure the rachis bridge area labeled with NMY-2::GFP in the time-lapse recordings shown in **Fig. 1H**, the center position of each apoptotic cell was obtained from the MorphographX tracking data and used to create a cropped .tiff-file with the apoptotic cell positioned in the image center, e.g. in **Fig. 1C**, allowing us to track cells over time. The rachis bridge opening and apical cell shape of the apoptotic cell and two neighboring cells, one at the distal and one at the proximal side, were outlined manually using Fiji software [70]. For each cell, a single z-plane was selected, which was used to measure the rachis bridge and the apical membrane area. Since the rachis bridge opening is only visible in very few planes and the gonads are not completely straight, the area of a part of the neighboring cells was sometimes determined in different z-sections. To minimize systematic errors, due to the fact that the apical surface is curved, apoptotic cells positioned in the middle of the gonads were selected for analysis as their apical surface is relatively flat.

Registration of cell positions

Variation in the positions of cells along the length of the gonad was decreased by a registration-like process: two cells far apart and located in the regular part of the tissue were selected and tracked throughout the movie. Cell positions were translated such that the position of the first cell changed linearly over time. This was achieved using a linear fit between the time and x-position of this first cell. Subsequently, the x-axis was scaled such that the distance between the first and second cell increased linearly over time and the position of the first cell was not changed. This scaling was based on a linear fit between time and distance between the first and second cell.

Measurement of rachis bridge areas in confocal image stacks

The areas of the rachis bridge were measured using Fiji software [70], as illustrated in **suppl. Fig. S3I**. Deconvolved or unprocessed confocal z-stacks were rotated and cropped to set the x-position (x=0) to the end of the gonad loop. The background was subtracted (rolling ball radius 50) and a Gaussian Blur (sigma r=1) was applied. The wand tool was used to manually select openings (black area) of the rachis bridges and their respective areas were measured with the Fiji built-in measurement function. If necessary, the tolerance of the wand tool was adjusted when selecting the openings. Since the rachis bridge of a cell is only visible in a few z-stacks, different z-stacks were selected for different cells.

Scripts used for image processing

script in Fijii used to crop and rotate single stacks (mgx preprocess.ijm, used only for single stacks analysis)

```
{
file=fileList[f];
if (!File.isDirectory(dir+file));
{
run("Bio-Formats Importer", "open="+dir+file+" windowless");
title=getTitle();
slices=nSlices;
run("Properties...", "unit=um pixel_width=0.2 pixel_height=0.2 voxel_depth=0.66");
run("Subtract Background...", "rolling=50 stack");
//run("Remove Outliers...", "radius=3 threshold=10 which=Bright stack");
run("Gaussian Blur...", "sigma=1 stack");
run("Subtract Background...", "rolling=50 stack");
setSlice(round(slices/2));
run("Enhance Contrast", "saturated=0.35");
setTool("line");
waitForUser("Draw a distal to proximal line.");
getLine(x1, y1, x2, y2, lineWidth);
lineAngle=atan2((y2-y1),(x2-x1));
rotateAngle=(-lineAngle+PI)/PI*180;
run("Rotate... ", "angle="+rotateAngle+" grid=0 interpolation=Bicubic enlarge stack");
setTool("polygon");
waitForUser("Crop the gonad");
run("Crop");
run("Clear Outside", "stack");
waitForUser("select the bottom layer");
bottom=getSliceNumber()-1;
waitForUser("select the top layer");
top=getSliceNumber()+1;
run("Slice Remover", "first="+top+" last="+slices+" increment=1");
run("Slice Remover", "first=1 last="+bottom+" increment=1");
setSlice(round(nSlices/2));
run("Enhance Contrast", "saturated=0.35");
path=resultDir+title+"_cropped.tif";
saveAs("Tiff", path);
close();
}
}
```

Script in Fijii to remove background from single stacks and germ cell tracking stacks (pipe_a_fiji_background.ijm)

```
showMessage("Choose the first file (must end with '1.tif') to subtract the background from. Other files must have
same naming convention.")
open("")
image_name = getInfo("image.filename")
core_input_name = split(image_name, "(1.tif)")
core_input_name = core_input_name[0]
input_directory = getInfo("image.directory")
close();
showMessage("Choose the last file (must start with "+core_input_name+") to subtract the background from.")
open("")
image_name = getInfo("image.filename")
```

```
last_number = split(image_name, "(.tif)")
last_number = split(last_number[0], "("+core_input_name+")")
last_number = last_number[1];
last_number = parseInt(last_number);
close();
target = getDirectory("Choose directory to save background-subtracted images to (eg meshes_etc)");

for (i=1; i<last_number+1; i++) {
        open(input_directory+"/"+core_input_name+i+".tif");
        run("Gaussian Blur...", "sigma=2 stack");
        run("Subtract Background...", "rolling=20 stack"); //changed from 10 to 20
        run("Remove Outliers...", "radius=2 threshold=50 which=Bright stack");
        run("StackReg", "transformation=[Rigid Body]");
        saveAs("Tiff", target+"/a_no_background_"+i+".tif");
        close();
        }
```

Script in Python to generate 2.5D projections and segmented cells in MorphographX (pipe_b_morphographx_segment)

```
"""Second step of segmentation and tracking of germline movies (with MorphoGraphX):
- It performs dilation and erosion steps to get rid of (most) signals that do not arise from germ cells before the turn
of the gonad.
- It creates a curved mesh (2.5D) through basal membranes
- It projects the image signal on this mesh and segments the projections by watershedding.
Prerequisites: folder with .tif files generated by pipe_a_fiji_background.ijm
Before running the code from MorphoGraphX, adjust the two paths in the first lines below
"""

srcDir= # folder containing the no_background files
targDir= # folder where to save the files
for i in range(1,2):
    Stack.Open(srcDir+'a_no_background_'+str(i)+'.tif', 'Main', '0')
    Global.SetCurrentStack('Main', '0')
    Stack.Binarize('10') #This variable is not always the same: wt, ced: 10; nmy2: 80 or 200
    Stack.Save(targDir+'b_binary_'+str(i)+'.tif', 'Work', '0', '5')
    Stack.Copy_Work_to_Main_Stack()
    Global.SetCurrentStack('Main', '0')
    Stack.Change_Voxel_Size('0.21', '0.21', '0.5')#depends on resolution movie/stacks
    Stack.Reverse_Axes('No', 'No', 'Yes')
    Stack.Copy_Work_to_Main_Stack()
    Global.SetCurrentStack('Work', '0')

##Get rid of background noise
    Stack.Erode('1', '1', '1', 'No')
    Stack.Dilate('1', '1', '1', 'No')

##Get rid of horizontal lines
    Stack.Dilate('12', '0', '0', 'No')
    Stack.Erode('0', '10', '0', 'No')
    Stack.Dilate('0', '10', '0', 'No')
    Stack.Combine_Stacks('Product')

##Get rid of vertical lines and structures that are not continuous in the x direction
    Stack.Copy_Work_to_Main_Stack()
    Stack.Dilate('12', '1', '0', 'No')
    Stack.Erode('25', '10', '0', 'No')
    Stack.Dilate('25', '10', '0', 'No')
    Stack.Open(srcDir+'a_no_background_'+str(i)+'.tif', 'Main', '1')
```

```
    Global.SetCurrentStack('Main', '1')
    Stack.Change_Voxel_Size('0.21', '0.21', '0.5')#depends on resolution movie/stacks
    Stack.Autoscale_Stack()
    Stack.Apply_Transfer_Function('0', '0', '0', '1')
    Stack.Reverse_Axes('No', 'No', 'Yes')
    Stack.Copy_Work_to_Main_Stack()
    Stack.Swap_or_Copy_Stack_1_and_2('Main', '1 <-> 2')
    Global.SetCurrentStack('Work', '0')
    Stack.Combine_Stacks('Product')

##Get rid of vertical lines that span the whole gonad
    Stack.Copy_Work_to_Main_Stack()
    Stack.Erode('0', '75', '0', 'No')#gonad no longer visible
    Stack.Dilate('0', '75', '0', 'No')
    Stack.Combine_Stacks('Subtract')
    Stack.Save(targDir+'c_gonad_only_'+str(i)+'.tif', 'Work', '0', '5')

##Edge detect
    Stack.Copy_Work_to_Main_Stack()
    Stack.Edge_Detect('70.0', '2.0', '0.3', '15000')
    Stack.Cimg_Median_Blur('3')
    #Close holes
    Stack.Dilate('25', '0', '0', 'No')
    Stack.Erode('25', '0', '0', 'No')

##Generate Mesh
    Stack.Copy_Work_to_Main_Stack()
    Mesh.Marching_Cubes_Surface('3', '5000')
    Mesh.Smooth_Mesh('12')
    Mesh.Subdivide()
    Mesh.Smooth_Mesh('10')
    Mesh.Subdivide()
    Mesh.Smooth_Mesh('10')

##Projecting the original image after background subtraction on mesh
    Stack.Open(srcDir+'a_no_background_'+str(i)+'.tif', 'Main', '0')
    Global.SetCurrentStack('Main', '0')
    Stack.Change_Voxel_Size('0.21', '0.21', '0.5')
    Stack.Autoscale_Stack()
    Stack.Apply_Transfer_Function('0', '0', '0', '1')
    Stack.Reverse_Axes('No', 'No', 'Yes')
    Stack.Copy_Work_to_Main_Stack()
    Global.SetCurrentStack('Work', '0')
    Mesh.Project_Signal('No', '0', '5', '0.0', '60000.0')
    Mesh.Difference_of_Gaussians('1.0', '5.0')

##Watershed segmentation of projected signal
    Mesh.Auto_Seeding('3.0')
    Mesh.Watershed_Segmentation('20000')
    Mesh.Fix_Corners('Yes', 'Yes', '5')

##For generating snapshots to check the quality and saving the mesh
    Mesh.Normalize_Signal('10')
    Global.Snapshot(targDir+'meshview_'+str(i)+'.png', 'false', '0', '0', '1.0', '95')
    Mesh.Save(targDir+'mesh_'+str(i)+'.mgxm', 'no', '0')

##If mesh quality was not satisfactory, the mesh was improved manually and projection and subsequent steps
were repeated
```

##In addition, segmentation was improved manually if necessary. In that case, that steps after the segmentation were repeated